isvr Institute of Sound and Vibration Research

Modelling Rail Roughness Growth on Tangent Tracks

X. Sheng, D.J. Thompson and C.J.C. Jones

ISVR Technical Memorandum No 929

March 2004

University of Southampton

SCIENTIFIC PUBLICATIONS BY THE ISVR

Technical Reports are published to promote timely dissemination of research results by ISVR personnel. This medium permits more detailed presentation than is usually acceptable for scientific journals. Responsibility for both the content and any opinions expressed rests entirely with the author(s).

Technical Memoranda are produced to enable the early or preliminary release of information by ISVR personnel where such release is deemed to the appropriate. Information contained in these memoranda may be incomplete, or form part of a continuing programme; this should be borne in mind when using or quoting from these documents.

Contract Reports are produced to record the results of scientific work carried out for sponsors, under contract. The ISVR treats these reports as confidential to sponsors and does not make them available for general circulation. Individual sponsors may, however, authorize subsequent release of the material.

UNIVERSITY OF SOUTHAMPTON

INSTITUTE OF SOUND AND VIBRATION RESEARCH

DYNAMICS GROUP

Modelling Rail Roughness Growth on Tangent Tracks

by

X. Sheng, D.J. Thompson and C.J.C. Jones

ISVR Technical Memorandum 929

March 2004

Authorised for issue by
Professor M.J. Brennan
Group Chairman

MODELLING RAIL ROUGHNESS GROWTH ON TANGENT TRACKS

X Sheng, D J Thompson and C J C Jones

ABSTRACT

Rail and wheel roughness including corrugation is one of the main sources of railway noise. A knowledge of how roughness grows and corrugation forms is vital for railway noise control at source. A countermeasure that reduces noise in the short term may actually increase noise in the long term if this measure contributes to roughness growth. In the past, intensive research has been performed on short-pitch rail corrugation. However for the track dynamics, most of the research employed the 'moving roughness model' in which the travelling of the wheel is replaced by the travelling of a roughness strip. Moreover, most of the research simplified the unsteady wheel/rail contact problem as a steady one and excluded the interactions between multiple wheels. These shortcomings have been overcome in the present study. Using the wavenumber-based calculation method for the response of a periodically supported rail to a moving harmonic load, dynamic wheel/rail forces are calculated for multiple wheels moving over an initially rough or smooth track. A two-dimensional unsteady contact mechanics theory is developed to evaluate the wear during the passage of the wheels, producing a changed roughness for the rail. A great number of repetitions of such a process demonstrate how rail roughness grows and corrugation forms.

CONTENTS

1. INTRODUCTION

When a wheel rolls over a rail, a contact patch of the size of a small coin is formed due to the local deformations of the wheel and rail around the contact point [1]. Due to the relative velocity (creep) and friction between the wheel and rail, the contact patch transmits not only normal stress, but also shear (tangential) stress. The stress in the contact patch may cause plastic deformation, material flow, rolling contact fatigue and wear (removal of material), leaving a changed, but likely rougher, railhead surface. The initial rail roughness grows after each passage of a wheel. In some situations, irregularities at some wavelengths grow, whereas others grow more slowly or remain unaffected or even suppressed. After several million wheel passages, a more or less regular pattern called rail corrugation may develop. Rail roughness and corrugation lead to increasing dynamic loads, and therefore reduce ride comfort, produce more vibration and noise. Therefore the control of roughness growth and corrugation formation is a major concern in the railway industry.

To understand the mechanisms of rail corrugation formation and to devise control measures, systematic studies including experimental as well as theoretical investigations have been performed in many countries. Up to now a huge number of papers have been published. Grassie and Kalousek [2] reviewed in 1993 more than 40 references on rail corrugation and classified corrugation into six groups according to their wavelength-fixing and damage mechanisms: (1) heavy haul corrugation (200-300 mm); (2) light rail corrugation (500-1500 mm); (3) booted sleepers type corrugation (45-60 mm); (4) contact fatigue corrugation (150-450 mm); (5) rutting corrugation (150-450 mm and 50 mm for trams); (6) roaring rail (or short pitch) corrugation (25-80 mm). Another more recent review (up to 2002) on rail corrugation studies was given in reference [3] including research carried out in Europe as well as in Japan. At the 6th International Conference on Contact Mechanics and Wear of Rail/Wheel Systems 2003, Grassie presented a new review paper [4] covering the progress in the last decade (1993-2003) on the understanding, measurement and treatment of corrugation. He concluded, amongst other things, that all types of corrugation identified to date are constant frequency rather than constant wavelength phenomena. For example, the pinned-pinned resonance of the track and the torsional vibration of a wheelset are two of the causes for corrugation formation. Previously it had been believed that short pitch corrugation was a constant wavelength phenomenon. He also pointed out that there is a strong circumstantial evidence that a close conformity of wheel and rail profiles exacerbates corrugation and this has not yet been demonstrated analytically.

Most of the recent work has been directed to modelling short pitch corrugation. Short pitch corrugation is commonly associated with high-speed, main-line track with relatively light axle loads. It occurs predominantly on tangent track or in gentle curves in which there is no contact between the wheel flange and the gauge face of the rail. Since the amplitude of short pitch corrugation is

relatively small, the main damage mechanism in its formation is believed to be the wear caused by the longitudinal slip between the wheel and rail at the slip zone of the contact patch. For train speeds between 20 and 70 m/s, short pitch corrugation gives rise to excitations predominantly in the frequency range of about 200 to 3000 Hz, coinciding with the frequency range of rolling noise. Therefore, in terms of railway rolling noise, short pitch corrugation is of greatest importance to the railway industry.

Müller [5], see also [6], following the studies by Valdivia [7], Hempelmann [8] and Frederick [9], presented a linear wheel-track model to predict instability and the formation of short pitch corrugation. The linearization is made around a reference state corresponding to a smooth railhead. A finite element model was used to model the dynamics of a single wheelset. The rail was described by an assembly of beams and plates. The rail was assumed to be infinitely long and discretely supported by sleepers. Both the vertical and lateral track dynamics have been included. A geometrical filter function due to the contact patch length was introduced which partly explains why corrugation wavelengths observed in practice vary little with train speeds.

To explore the wavelength-fixing mechanism for short pitch corrugation, Nielsen [10] conducted a study for a cylinder rolling on a sinusoidal rail profile without any influence of wheel/track dynamics. By extending the Hertzian contact theory for the normal contact stress and Carter's solution [11] for the tangential contact stress, the wear due to wheel/rail slip in the longitudinal direction was calculated. It was shown that sinusoidal irregularities increase preferentially in a particular wavelength range. In other words, the wavelength-fixing mechanism may partly exist in the contact mechanics. A similar problem was also considered previously by Piotrowski [12] and Kalker [13].

Heike Ilias [14] provides an approach in the time-domain to the rail corrugation problem in which non-linearity of the contact mechanics is taken into account as well as transient structural dynamics within the long-term wear process. A viscously damped track model is used. The influence of railpad stiffness on corrugation growth is addressed. Starting with measured rail profiles it is found from calculations that corrugations grow more quickly with stiffer railpads. In addition, a novel influence of the sleeper passing frequency is demonstrated: for the chosen parameters and the very small initial roughness, parametric excitation from the discrete supports dominates the final profile.

The models mentioned above consider only a single wheel or wheelset, excluding effects from neighbouring wheels. Wu and Thompson [15] have demonstrated the great effect of the presence of multiple wheelsets in a bogie on the normal contact forces. They also presented an

investigation of rail corrugation generation by combining the multiple wheel/rail dynamics (vertical only), a quasi-static two-dimensional contact mechanics model and wear process [16].

Most of the models are formulated in the frequency domain although several are found working in the time domain [14, 17]. Time-domain models require the infinitely long track to be truncated, which may cause wave reflections from the ends if the railpad is very soft [14]. It is our belief that a frequency-domain model is more useful to give insight into the mechanisms involved in corrugation formation and roughness growth.

It is worth pointing out that, in all the aforementioned frequency-domain models, the motion of the wheel along the rail is replaced by the motion of an 'irregularity strip' between the wheel and rail. Thus the effect of the wheel speed cannot be taken into account. It has been shown in references [18] and [19] that the wheel speed can have significant effects on wheel/rail interactions when the excitation frequency is close to the pinned-pinned frequency which, as revealed by previous studies, is important to corrugation formation.

In the study of rail roughness growth and rail corrugation formation, it is vital to know the tangential stress distribution in the contact patch and the slip velocity between the wheel and rail in the slip zone. In steady rolling contact problems, in which the contact force and the contact geometry are time-invariant, calculation methods have been well established [20, 21], and analytical formulae are available for two-dimensional problems [11]. It is noticed that all the aforementioned models simplify the contact problem as a steady one. However in practice, due to the presence of short-wavelength roughness, the rolling contact is strongly unsteady. A minimum principle has been described by Kalker [22] for two-dimensional steady and unsteady rolling contact problems.

This report presents a new effort on rail roughness growth, trying to overcome the shortcomings in previous studies. Using the wavenumber-based calculation method derived in reference [18] for the response of a periodically supported rail to a moving harmonic load, dynamic wheel/rail forces are calculated for multiple wheels moving over an initially rough or smooth track. A two-dimensional unsteady contact mechanics theory is developed to evaluate the wear during the passage of the wheels, producing a changed roughness for the rail. A great number of repetitions of such a process will demonstrate how rail roughness grows and corrugation forms. In Section 2, the accuracy is discussed of using half-space theory to approximate the deformation in a contact patch. Section 3 presents a calculation method for the response of a half-space subject to a harmonic load and demonstrates that damping may be introduced into a contact spring. Section 4 deals with two-dimensional dynamic wheel/rail contact problems. Having worked out the tangential stress and slip velocity between the wheel and rail in the contact patch, wear can be evaluated numerically using a

simple wear law. This is shown in Section 5. Section 6 presents some results to identify the effects of various parameters on rail roughness growth and rail corrugation formation.

2. TWO DISPLACEMENT COMPONENTS IN THE CONTACT ZONE

In what follows, it is shown that at positions close to a dynamic load applied in a small area, the displacement of an elastic body can be divided into two components, one of which is that of the corresponding half-space. Figure 1 shows an elastic body, the boundary of which is denoted by Γ, of which a small part, denoted by Γ_ε, coincides (due to contact with another elastic body not shown) with the surface of a half-space. The elastic body is subject to harmonic tractions of frequency $\omega, \mathbf{p}(\mathbf{y},\omega)$, on Γ_ε only, where, $\mathbf{y} \in \Gamma_\varepsilon$. From the Betti reciprocal theorem [23], the displacement at any position $\mathbf{x}$ is given by an integral over the whole boundary of the elastic body,

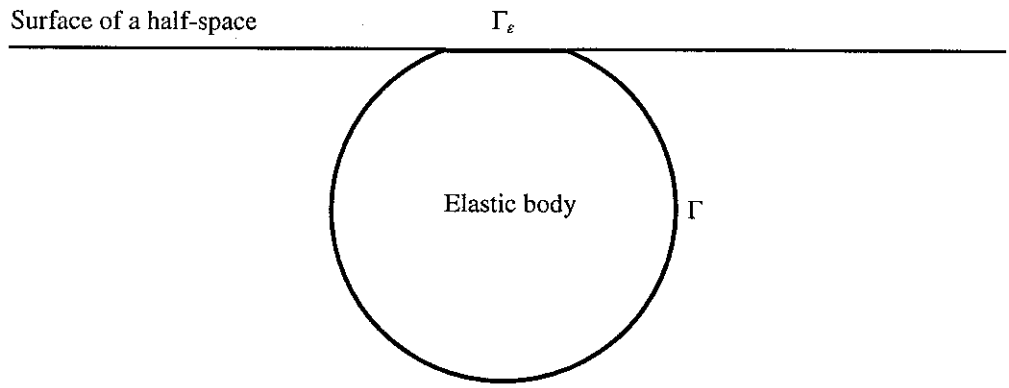

Figure 1. An elastic body with a small part of its boundary on the surface of a half-space.

$$\mathbf{C}(\mathbf{x})\mathbf{u}(\mathbf{x},\omega) = \int_\Gamma \mathbf{U}^T(\mathbf{y},\omega;\mathbf{x})\mathbf{p}(\mathbf{y},\omega)d\Gamma - \int_\Gamma \mathbf{P}^T(\mathbf{y},\omega;\mathbf{x})\mathbf{u}(\mathbf{y},\omega)d\Gamma \qquad (1)$$

where, $\mathbf{u}(\mathbf{y}, \omega)$ and $\mathbf{p}(\mathbf{y}, \omega)$ are displacement and traction vectors on the boundary of the elastic body, $\mathbf{U}(\mathbf{y},\omega;\mathbf{x})$ and $\mathbf{P}(\mathbf{y},\omega;\mathbf{x})$ are displacement and traction Green's function matrices of the half-space, with the source at $\mathbf{x}$ and observer at $\mathbf{y}$, and finally, $\mathbf{C}(\mathbf{x})$ is a matrix determined solely by the geometry of the boundary at $\mathbf{x}$. Since externally applied tractions, denoted by $\mathbf{p}(\mathbf{y},\omega)$, exist only on Γ_ε, equation (1) becomes

$$\mathbf{C}(\mathbf{x})\mathbf{u}(\mathbf{x},\omega) = \int_{\Gamma_\varepsilon} \mathbf{U}^T(\mathbf{y},\omega;\mathbf{x})\mathbf{p}(\mathbf{y},\omega)d\Gamma - \int_{\Gamma_\varepsilon} \mathbf{P}^T(\mathbf{y},\omega;\mathbf{x})\mathbf{u}(\mathbf{y},\omega)d\Gamma - \int_{\Gamma-\Gamma_\varepsilon} \mathbf{P}^T(\mathbf{y},\omega;\mathbf{x})\mathbf{u}(\mathbf{y},\omega)d\Gamma \qquad (2)$$

If $\mathbf{y} \in \Gamma_\varepsilon$, then $\mathbf{P}^T(\mathbf{y},\omega;\mathbf{x})$ is non-vanishing only when $\mathbf{x} = \mathbf{y}$. The term on the left-hand side combined with the second integral on the right-hand side gives the displacement $\mathbf{u}(\mathbf{x},\omega)$ for $\mathbf{x} \in \Gamma_\varepsilon$. Therefore when $\mathbf{x} \in \Gamma_\varepsilon$,

$$\mathbf{u}(\mathbf{x},\omega) = \int_{\Gamma_\varepsilon} \mathbf{U}^T(\mathbf{y},\omega;\mathbf{x})\mathbf{p}(\mathbf{y},\omega)d\Gamma - \int_{\Gamma-\Gamma_\varepsilon} \mathbf{P}^T(\mathbf{y},\omega;\mathbf{x})\mathbf{u}(\mathbf{y},\omega)d\Gamma \tag{3}$$

Since $\mathbf{U}^T(\mathbf{y},\omega;\mathbf{x}) = \mathbf{U}(\mathbf{x},\omega;\mathbf{y})$, equation (3) becomes

$$\mathbf{u}(\mathbf{x},\omega) = \int_{\Gamma_\varepsilon} \mathbf{U}(\mathbf{x},\omega;\mathbf{y})\mathbf{p}(\mathbf{y},\omega)d\Gamma - \int_{\Gamma-\Gamma_\varepsilon} \mathbf{P}^T(\mathbf{y},\omega;\mathbf{x})\mathbf{u}(\mathbf{y},\omega)d\Gamma \qquad (\mathbf{x}\in\Gamma_\varepsilon) \tag{4}$$

Equation (4) indicates that, the displacement in the contact zone can be divided into two components. The first component is given by the first integral and is identical to the displacement of the half-space. This component is termed *the local displacement* and is strongly dependant on the position in the contact patch. The second component is determined by the second integral and is produced by the displacement, $\mathbf{u}(\mathbf{y},\omega)$, on the boundary $\Gamma-\Gamma_\varepsilon$. This component is termed *the global displacement* and can be regarded as constant cross the contact patch. The first component provides the basis for the introduction of the Hertz contact spring and the calculation of the geometry of the contact zone. If the body is modelled as a rigid body, then the second component is given by $\frac{-1}{M\omega^2}\mathbf{P}_0$, where M is the mass of the body and $\mathbf{P}_0$ is the contact force (amplitude) vector. If a finite element model with a mesh of size similar to the contact patch is used to model the elastic body, then part of the local deformation of the body at the contact point may have been included in this finite element model. The addition of a contact spring based on the Hertz theory to the receptance calculated from the FE model for the contact point may exaggerate the response at the contact point. In this case, in order to keep the contact spring, the receptance from the FE model must be modified according to equation (4). If the contact point is node 1, then the FE equation of the elastic body is given by

$$\left(-\mathbf{M}\omega^2 + \mathbf{K}\right)\mathbf{u}(\omega) = \begin{Bmatrix} \mathbf{P}_0 \\ \vdots \\ 0 \end{Bmatrix} \tag{5}$$

where, $\mathbf{M}$ and $\mathbf{K}$ are the mass and stiffness matrices and $\mathbf{P}_0$, according to the FEM, is the resultant of the traction in the contact area and is applied at node 1. From this equation the displacement at each node can be worked out. It is assumed that only at node 1 the displacement is not sufficiently accurate. The true value of the displacement at node 1 is given by equation (4). As has been identified, the second component in equation (4) is the displacement at node 1 which is produced by the displacements of the other nodes on the boundary of the elastic body. Thus the second component in equation (4) may be approximated by the average of the displacements of the nodes next to node 1 on the boundary of the elastic body. This average, rather than the displacement

worked out from equation (5) for node 1, should be used as the receptance of the elastic body at the contact point, if the Hertz contact spring is introduced.

3. DISPLACEMENT OF THE HALF-SPACE

To evaluate the first component in equation (4), the displacement at the half-space surface due to a point harmonic load is required. An elastic half-space, described by Young's modulus E, Possion ratio ν and density ρ, is subjected to a vertical point harmonic load $Pe^{i\omega t}$ at the origin on the surface. The Lamé constants are given by

$$\lambda = \frac{\nu E}{(1+\nu)(1-2\nu)},\ \mu = \frac{E}{2(1+\nu)} \tag{6}$$

and the P- and S-wave speeds are given by

$$c_1 = \sqrt{(\lambda + 2\mu)/\rho}\ ,\ c_2 = \sqrt{\mu/\rho} \tag{7}$$

Defining

$$\alpha_1 = \sqrt{\beta^2 - \omega^2/c_1^2}\ ,\ \alpha_2 = \sqrt{\beta^2 - \omega^2/c_2^2} \tag{8}$$

$$G(\beta,\omega) = \frac{\alpha_1\omega^2}{\mu c_2^2[4\alpha_1\alpha_2\beta^2 - (2\beta^2 - \omega^2/c_2^2)^2]} \tag{9}$$

where, β is the wavenumber in the radial direction, then the vertical displacement amplitude at a distance, r, from the loading point is given by [24]

$$w(r) = \frac{P}{2\pi}\int_0^\infty G(\beta,\omega)J_0(\beta r)\beta d\beta \tag{10}$$

where, $J_0(\beta r)$ is the Bessel function of the first kind of order zero.

The Rayleigh equation is obtained by setting the dominator of G in equation (9) equal to zero, *i.e.*

$$4\alpha_1\alpha_2\beta^2 - (2\beta^2 - \omega^2/c_2^2)^2 = 0 \tag{11}$$

At a given frequency ω, the real and positive root of this equation, denoted by β_R, is the Rayleigh wavenumber. The Rayleigh wave speed is determined by $c_R = \omega/\beta_R$. Equation (11) is equivalent to

$$\left(\frac{c_R}{c_2}\right)^6 - 8\left(\frac{c_R}{c_2}\right)^4 + 8\left(\frac{2-\nu}{1-\nu}\right)\left(\frac{c_R}{c_2}\right)^2 - \frac{8}{1-\nu} = 0 \tag{12}$$

Since at β_R the integrand in equation (10) is singular, numerical integration algorithms cannot be applied directly to evaluate this integral. It can be written out

$$w(r) = \frac{P}{2\pi}\int_0^{\infty} G(\beta,\omega)J_0(\beta r)\beta d\beta$$
$$= \frac{P}{2\pi}\int_0^{\beta_R} G(\beta,\omega)J_0(\beta r)\beta d\beta + \frac{P}{2\pi}\int_{\beta_R}^{2\beta_R} G(\beta,\omega)J_0(\beta r)\beta d\beta + \frac{P}{2\pi}\int_{2\beta_R}^{\infty} G(\beta,\omega)J_0(\beta r)\beta d\beta \quad (13)$$

Letting $\beta = -\beta' + 2\beta_R$ in the second integral gives

$$\int_{\beta_R}^{2\beta_R} G(\beta,\omega)J_0(\beta r)\beta d\beta = -\int_{\beta_R}^{0} G(2\beta_R - \beta',\omega)J_0[(2\beta_R - \beta')r](2\beta_R - \beta')d\beta'$$
$$= \int_0^{\beta_R} G(2\beta_R - \beta',\omega)J_0[(2\beta_R - \beta')r](2\beta_R - \beta')d\beta'$$
$$= \int_0^{\beta_R} G(2\beta_R - \beta,\omega)J_0[(2\beta_R - \beta)r](2\beta_R - \beta)d\beta$$

thus equation (13) becomes

$$w(r) = \frac{P}{2\pi}\int_0^{\beta_R}\left[G(\beta,\omega)J_0(\beta r)\beta + G(2\beta_R - \beta,\omega)J_0[(2\beta_R - \beta)r](2\beta_R - \beta)\right]d\beta$$
$$+ \frac{P}{2\pi}\int_{2\beta_R}^{\infty} G(\beta,\omega)J_0(\beta r)\beta d\beta \quad (14)$$

Now the singularities appearing in the integrand of the first integral cancel. This is demonstrated in Figure 2. For this figure and other results, unless otherwise indicated, the material properties are taken for a rail, *i.e.*, $E = 2.1\times10^{11}$ N/m^2, $\nu = 0.3$, $\rho = 7850$ kg/m^3, $r = 0.005$ m and $f = \frac{\omega}{2\pi} = 4000$ Hz. The Rayleigh wavenumber is 8.448 rad/m. Figure 2 shows that, for wavenumbers less than the Rayleigh wavenumber, three intervals can be identified: from zero to the P-wavenumber, $\beta_1 = 4.188$ rad/m; and then up to the S-wavenumber, $\beta_2 = 7.835$ rad/m; and then up to the Rayleigh wavenumber. Within each interval, the integrand in the first integral of equation (14) is a smooth function and the integral over this interval can be performed using a conventional numerical algorithm.

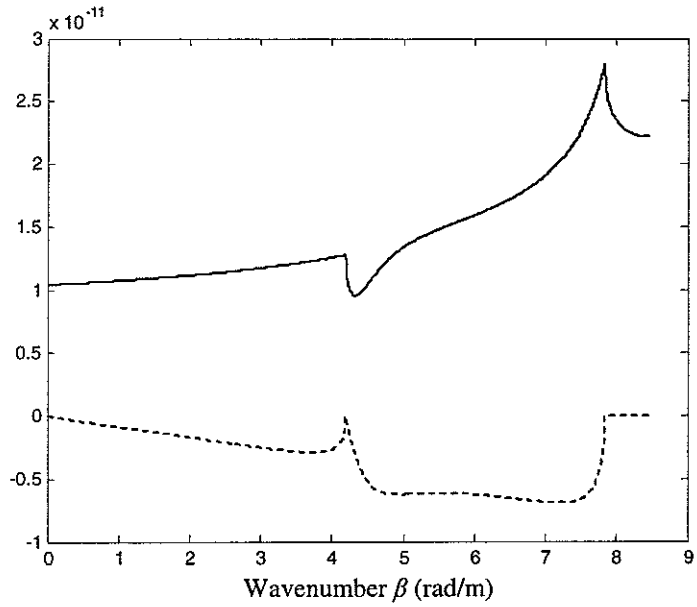

Figure 2. The real (——) and imaginary (– – –) parts of the integrand in the first integral of equation (14).

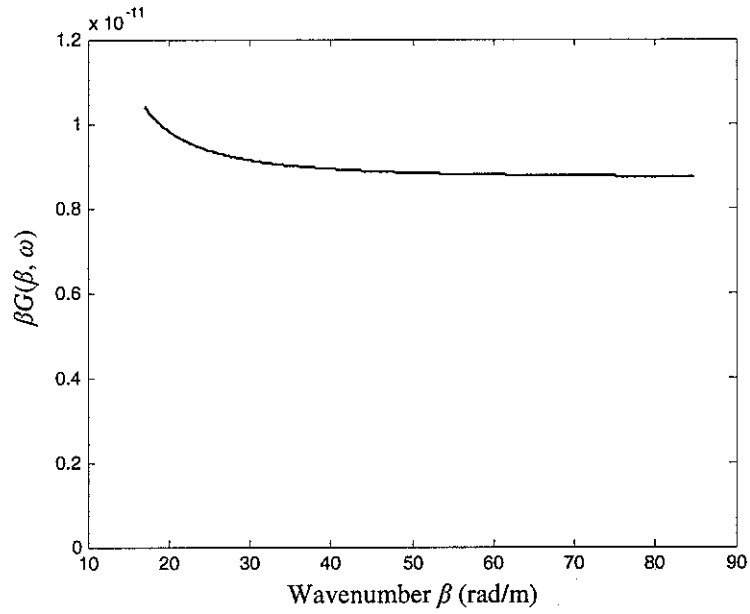

Figure 3. Function βG plotted against wavenumber for $\beta > 2\beta_R$.

The function $\beta G(\beta,\omega)$ is plotted in Figure 3 for $\beta \geq 2\beta_R$. It can be seen as the wavenumber increases, this function approaches a constant. In fact from equation (9) it can be shown that

$$\lim_{\beta\to\infty} \beta G(\beta,\omega) = \lim_{\omega\to 0} \beta G(\beta,\omega) = \frac{1}{2\mu(1-c_2^2/c_1^2)} = \frac{2(1-\nu^2)}{E} \tag{15}$$

and for $\beta \geq 10\beta_R$, the function $\beta G(\beta,\omega)$ can be approximated by this limit.

Now equation (14) can be written as (note: $\int_0^\infty J_0(x)dx = 1$)

$$
\begin{aligned}
w(r) = \frac{P}{2\pi}\int_0^{\beta_1}&[G(\beta,\omega)J_0(\beta r)\beta + G(2\beta_R-\beta,\omega)J_0[(2\beta_R-\beta)r](2\beta_R-\beta)]d\beta \\
+\frac{P}{2\pi}\int_{\beta_1}^{\beta_2}&[G(\beta,\omega)J_0(\beta r)\beta + G(2\beta_R-\beta,\omega)J_0[(2\beta_R-\beta)r](2\beta_R-\beta)]d\beta \\
+\frac{P}{2\pi}\int_{\beta_2}^{\beta_R}&[G(\beta,\omega)J_0(\beta r)\beta + G(2\beta_R-\beta,\omega)J_0[(2\beta_R-\beta)r](2\beta_R-\beta)]d\beta \\
+\frac{P}{2\pi}\int_{2\beta_R}^{10\beta_R}&G(\beta,\omega)J_0(\beta r)\beta d\beta + \frac{(1-\nu^2)P}{\pi E r}\left(1-\int_0^{10\beta_R r}J_0(x)dx\right)
\end{aligned}
\tag{16}
$$

For a static load with $\omega = 0$, from equation (16) the Boussinesq formula is obtained

$$
w(r) = \frac{(1-\nu^2)P}{\pi E r} \tag{17}
$$

Equation (16) shows that, for small r, the displacement amplitude consists mainly of the component given by equation (17), i.e., the Boussinesq solution. This is illustrated in Figure 4 in which the vertical displacement amplitude (the real part) produced by a unit load (P =1 N) of frequency 4000 Hz is plotted against the distance between the observer and the loading point. Equation (16) gives the same results as those from equation (17) for the indicated range of observers. In other words, the static contact mechanics can be applied to deal with dynamic contact problems. However, equation (16) gives a small imaginary part caused by energy (power) radiation into the half-space (no material damping is considered here). The radiated power is identical to the power done by the load, *i.e.*, $\frac{-1}{2}P^2\omega\,\mathrm{Im}(w^0(0))$, where $\mathrm{Im}(w^0(0))$ is the imaginary part of the displacement produced by a unit load at the loading point and its value is finite although the real part is infinite. The radiated power for different frequencies is shown in Figure 5; it increases non-linearly with frequency. When a Hertz contact spring is inserted between a wheel and rail, a loss factor may be introduced to dissipate energy equivalent to that radiated into two half-spaces representing the wheel and rail. The complex stiffness of the contact spring is denoted by $k_H(1+i\eta_H)$, and the energy dissipated by the spring is given by $\frac{1}{2}P^2\omega\eta_H k_H^{-1}$. Letting $\frac{1}{2}P^2\omega\eta_H k_H^{-1} = 2\times\frac{-1}{2}P^2\omega\,\mathrm{Im}(w^0(0))$ gives $\eta_H = -2k_H\,\mathrm{Im}(w^0(0))$. Contact spring loss factor is proportional to the contact stiffness which is determined not only by the static contact load, but also by the contact geometry. Figure 6 shows the contact spring loss factor at different frequencies for $k_H = 1.4\times10^9$ N/m. It can be seen that the loss factor is linearly frequency-dependent.

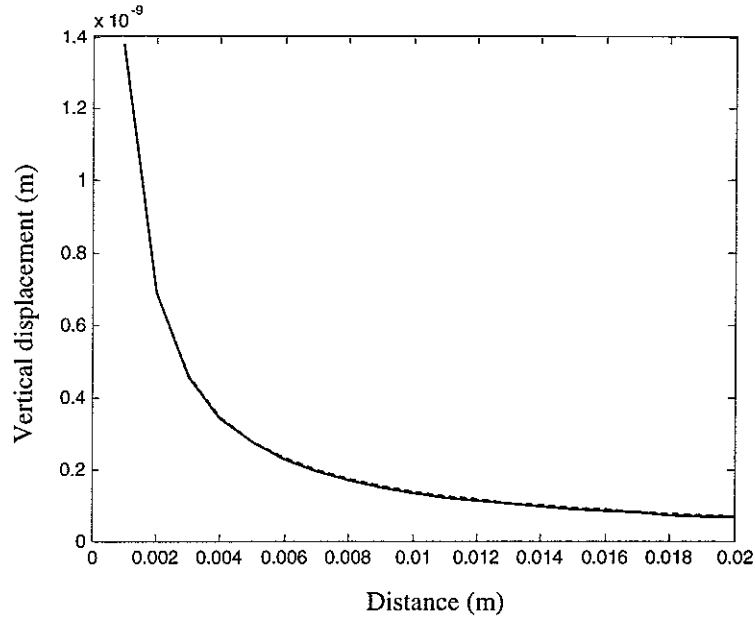

Figure 4. Vertical displacement amplitude produced by a unit load of 4000 Hz. ——, real part from equation (16); – – –, from equation (17).

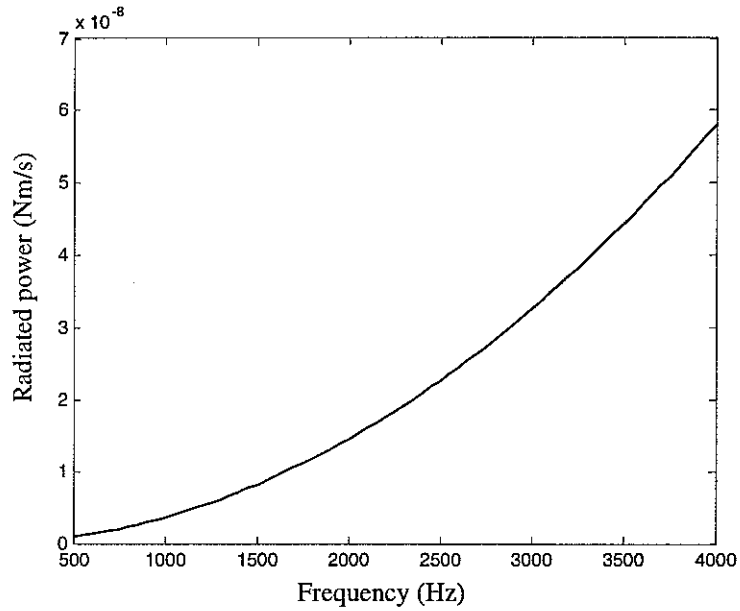

Figure 5. Power radiated into the half-space subject to a unit vertical harmonic load of different frequencies.

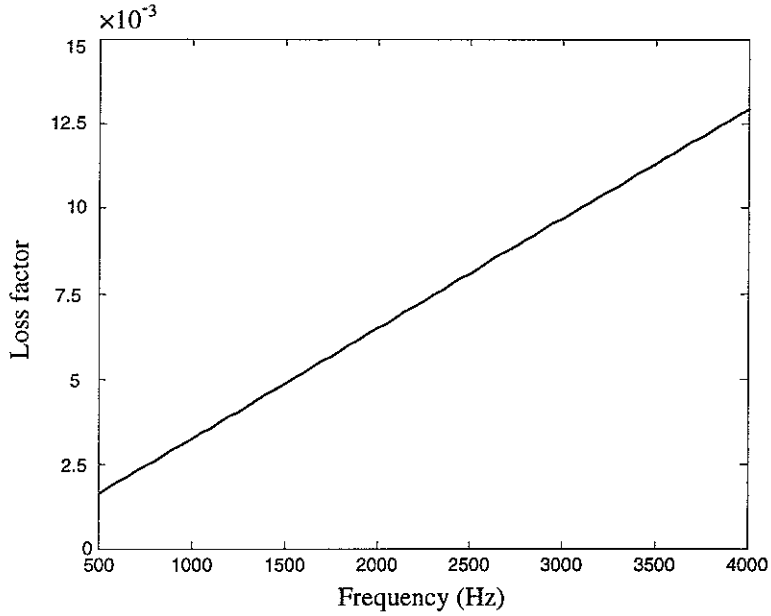

Figure 6. Loss factor of the contact spring at different frequencies. The stiffness of the spring is 1.4×10^9 N/m.

4. TWO-DIMENSIONAL DYNAMIC WHEEL/RAIL CONTACT

4.1 RAIL ROUGHNESS

The contact mechanics of a wheel/rail system is simplified to a two-dimensional rolling contact problem in which a cylindrical wheel of radius R_W is rolling uniformly at speed V over an irregular rail profile. The vertical profile of the railhead is described by

$$z(x)=\sum_{k=1}^{\infty}\left[A_k\cos(k\beta_0 x)+B_k\sin(k\beta_0 x)\right]=\sum_{k=-\infty}^{\infty}Z_k e^{ik\beta_0 x} \tag{18}$$

and is directed upwards, where, $i=\sqrt{-1}$, $\beta_0=\frac{2\pi}{L}$ with L denoting the sleeper spacing, $Z_0=0$, and

$$Z_k=\tfrac{1}{2}(A_k-iB_k),\ Z_{-k}=\tfrac{1}{2}(A_k+iB_k),\ k=1,2,\ldots \tag{19}$$

It has been assumed in equation (18) that the profile is a periodic function of x with the period equal to the sleeper spacing. At time t the lth wheel in a bogie (or a train) arrives at position $x=a_l+Vt$, where a_l denotes the initial position of this wheel. The curvature of the rail profile at this wheel position is given by

$$\kappa(t)\approx -z''(x)=\sum_{k=-\infty}^{\infty}(k\beta_0)^2 Z_k e^{ik\beta_0 x}=\sum_{k=-\infty}^{\infty}(k\beta_0)^2 Z_k e^{ik\beta_0 a_l}e^{ik\Omega_0 t} \tag{20}$$

where, $\Omega_0=\beta_0 V$ is the sleeper-passing frequency in radians per second. The negative sign before $z''(x)$ is introduced to make the curvature positive if the curvature centre is located underneath the rail rolling surface. This is required by the Hertz contact theory.

4.2 NORMAL WHEEL/RAIL CONTACT FORCE AND STRESS

For a single or multiple wheels moving along the rail profile given by equation (18), a calculation method has been derived in reference [19] for the normal wheel/rail contact forces. The lth normal wheel/rail force is expressed as

$$P_l(t) = \sum_{k=-\infty}^{\infty} P_{lk} e^{ik\Omega_0 t} \tag{21}$$

where P_{l0} equals half the lth axle load. Since the normal contact forces and the contact geometry are time (or position) dependent, the rolling contact becomes unsteady. However, as has been shown in the last section, the Boussinesq formula is still valid for a dynamic force. Therefore the Hertz theory is applicable here to determine the normal contact stress (pressure) which is given by [1]

$$p_l(\xi, t) = \frac{P_l(t)}{\pi a(t) b} \sqrt{1 - \left(\xi / a(t)\right)^2} \tag{22}$$

where ξ is the local coordinate within the contact patch (see Figure 7), $2b$ is the wheel width (in contact) and $2a(t)$ is the contact patch length in the rolling direction of the wheel,

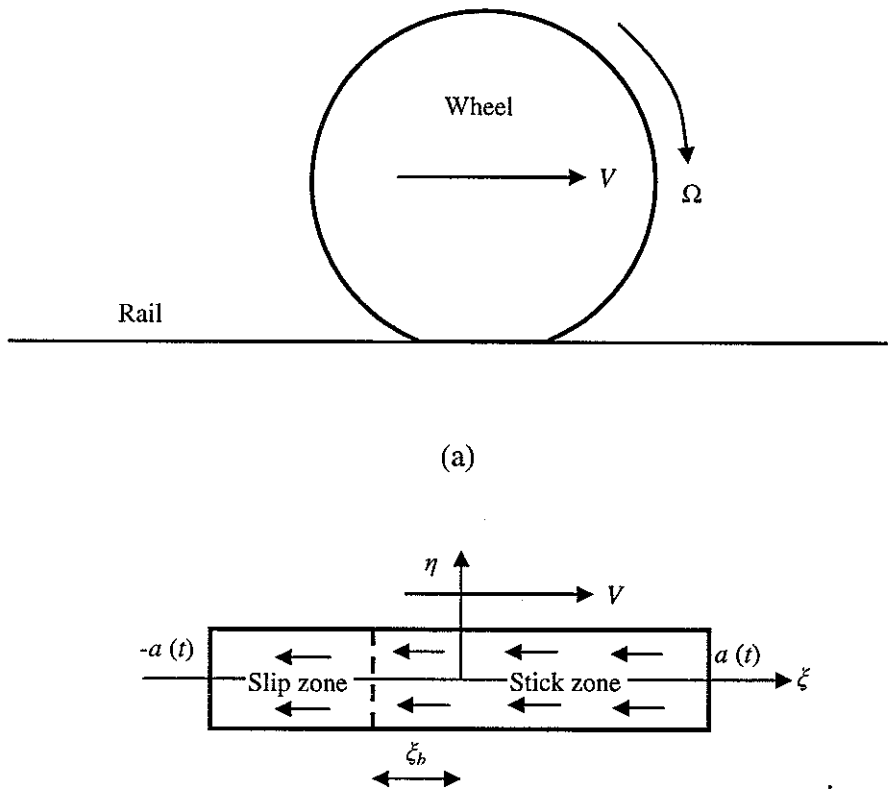

Figure 7. (a) Wheel/rail rolling contact; (b) contact patch on the rail and the tangential stress.

$$a(t) = \sqrt{\frac{4(1-\nu^2)P_l(t)R(t)}{\pi b E}} \tag{23}$$

in which $R(t)$ is the equivalent radius of the wheel/rail contact and is determined by

$$\frac{1}{R(t)} = \frac{1}{R_W} + \kappa(t) \tag{24}$$

It can be seen that both the normal contact stress and the length of the contact patch are periodic functions of time with period equal to the sleeper-passing time. Equation (24) requires that $z''(x) < 1/R_W$, otherwise multiple contact occurs between the wheel and the rail.

4.3 TANGENTIAL WHEEL/RAIL CONTACT STRESS AND SLIP VELOCITY

In general there is creep, that is the rigid relative velocity in the contact zone, between the wheel and rail. For a two-dimensional rolling contact problem, creep exists only in the longitudinal direction. The longitudinal creep ratio or creepage is defined as

$$\gamma_1 = \frac{V - \Omega R_W}{V} \tag{25}$$

where, Ω is the rotation velocity of the wheel. For a locomotive wheel subject to a driving torque, the longitudinal creepage defined by equation (25) must be *negative*. In the contact patch, materials of the wheel and rail experience elastic deformation. This deformation consists of two components, the local deformation and the global deformation, as indicated by equation (4). The longitudinal local relative displacement *between the wheel and rail, i.e.* the displacement of the wheel minus that of the rail (each kinetic quantity is defined based on the coordinate system shown in Figure 7) in the contact patch is denoted by $u(\xi,t)$. The longitudinal global relative displacement between the wheel and rail is denoted by $\bar{u}(t)$, which, as indicated by the notation, is independent of the local coordinate ξ. $\bar{u}(t)$ may be evaluated in terms of the contact force and dynamics of the wheel and rail at the contact point. If the wheel is modelled as a rigid body without torsional vibration and the rail is modelled as a beam with no longitudinal flexibility, then $\bar{u}(t) = 0$. Thus the relative velocity (slip velocity) between the wheel and rail in the contact patch can be written as [1]

$$s(\xi,t) = V\gamma_1 - V\frac{\partial u(\xi,t)}{\partial \xi} + \frac{\partial u(\xi,t)}{\partial t} \tag{26}$$

The contact patch may be divided into slip zones and stick zones. In the slip zones, the slip velocity is different from zero and the tangential stress $q(\xi,t)$ reaches the maximum frictional stress, *i.e.*,

$$q(\xi,t) = -\mu_d\, p(\xi,t)\frac{s(\xi,t)}{|s(\xi,t)|},\ s(\xi,t) \neq 0, \text{ in slip zones} \tag{27}$$

where, μ_d is the dynamic friction coefficient. In the stick zones,

$$|q(\xi,t)| \leq \mu_s p(\xi,t),\ s(\xi,t)=0,\ \text{in stick zones} \tag{28}$$

where $\mu_s \geq \mu_d$ denotes the static friction coefficient.

Constitutive equations connecting the tangential stress and local relative displacement are given by [1]

$$u(\xi,t) = -\frac{4(1-\nu^2)}{\pi E}\int_{-a(t)}^{a(t)} q(\varsigma,t)\ln\left|1-\frac{\xi}{\varsigma}\right|d\varsigma + u(0,t) \tag{29}$$

Derivatives of $u(\xi,t)$ with respect to ξ and t are given by

$$\frac{\partial u(\xi,t)}{\partial \xi} = -\frac{4(1-\nu^2)}{\pi E}\int_{-a(t)}^{a(t)} q(\varsigma,t)\frac{1}{\xi-\varsigma}d\varsigma \tag{30}$$

$$\frac{\partial u(\xi,t)}{\partial t} = -\frac{4(1-\nu^2)}{\pi E}\int_{-a(t)}^{a(t)} \frac{\partial q(\varsigma,t)}{\partial t}\ln\left|1-\frac{\xi}{\varsigma}\right|d\varsigma + \frac{\partial u(0,t)}{\partial t} \tag{31}$$

In the derivation of equation (31), the fact has been taken into account that at the leading and trailing edges of the contact patch the tangential stress must vanish. Due to the fundamental defect of the two-dimensional half-space model, the relative displacement $u(\xi,t)$ cannot be determined by equation (29) only, since $u(0,t)$ remains unknown. An extra condition must be introduced. This extra condition must be chosen according to the mechanics of the real contacting bodies, rather than two 2D half-spaces. Johnson [1] replaces $u(0,t)$ by the displacement at the centre of the rectangular area $2a(t)\times 2b$ in which the total tangential contact force is uniformly distributed. In the present work, the elastic foundation model is used to approximate the displacement $u(0,t)$, *i.e.*,

$$u(0,t) = \frac{q(0,t)}{\sigma} \tag{32}$$

where, σ is the tangential stiffness at the centre of the contact patch and is given by [25]

$$\sigma = \frac{1}{16}\left[\frac{b}{P_t(t)R(t)}\left(\frac{\pi E}{1-\nu^2}\right)^3\right]^{1/2} \tag{33}$$

Equations (26) to (33) define the so-called unsteady tangential rolling contact problem in which the tangential stress $q(\xi,t)$ and the slip velocity $s(\xi,t)$ are to be found. Unlike the 2D steady rolling contact problem, no analytical solution is available to the unsteady tangential rolling contact problem. However numerical methods such as Linear Programming proposed by Kalker [22] have been developed for this problem.

According to Carter's solution [11], the contact patch for steady rolling is divided into a single stick zone and a single slip zone. In the slip zone which is the trailing part of the patch the slip velocity does not change its sign. In the present work it is assumed that the amplitude of the rail roughness is not great enough to alter these features (Figure 7), although the length of the contact patch and the stick-slip dividing line are time-dependent. Under this assumption a method is derived for the unsteady rolling contact problem and is described below.

The maximum value of $a(t)$ is denoted by $a_{\max}$. A number, N, of nodes are evenly allocated over a *nominal contact patch* defined by $\Gamma = [-a_{\max}, a_{\max}]$, where N is an *odd* integer. The length between adjacent nodes is determined by

$$\Delta_\xi = 2a_{\max}/(N-1) \tag{34}$$

and the coordinates of the nodes are given by

$$\xi_m = -a_{\max} + (m-1)\Delta_\xi \ , \ (m = 1, 2, \cdots, N) \tag{35}$$

The tangential stress will be calculated at these nodes (therefore they are termed *the stress nodes*) and between any adjacent nodes the stress is assumed to be linear. The stress at this node must be set to zero if a node is outside the contact patch. In addition to the stress nodes, a second set of $N-1$ nodes (called *the displacement nodes*) is similarly defined for the evaluation of the relative displacement:

$$\xi'_m = \xi_m + \Delta_\xi / 2 \ , \ (m = 1, 2, \cdots, N-1) \tag{36}$$

Equation (36) shows that each displacement node is located mid-way between two adjacent stress nodes.

Now equation (29) can be approximated by

$$\begin{aligned} u(\xi'_m, t) &= -\frac{4(1-\nu^2)}{\pi E} \sum_{n=1}^{N-1} \int_{\xi_n}^{\xi_{n+1}} \left\{ \begin{array}{l} q(\xi_n, t) \\ + \dfrac{1}{\Delta_\xi}[q(\xi_{n+1}, t) - q(\xi_n, t)](\varsigma - \xi_n) \end{array} \right\} \ln\left|1 - \frac{\xi'_m}{\varsigma}\right| d\varsigma + u(0,t) \\ &= -\frac{4(1-\nu^2)}{\pi E} \sum_{n=1}^{N-1} \left\{ \begin{array}{l} q(\xi_n, t) \displaystyle\int_{\xi_n}^{\xi_{n+1}} \ln\left|1 - \frac{\xi'_m}{\varsigma}\right| d\varsigma \\ + \dfrac{1}{\Delta_\xi}[q(\xi_{n+1}, t) - q(\xi_n, t)] \displaystyle\int_{\xi_n}^{\xi_{n+1}} (\varsigma - \xi_n) \ln\left|1 - \frac{\xi'_m}{\varsigma}\right| d\varsigma \end{array} \right\} + u(0,t) \end{aligned} \tag{37}$$

It can be shown that for $\varsigma \neq 0$

$$\int_{\xi_n}^{\xi_{n+1}} \ln\left|1-\frac{\xi'_m}{\varsigma}\right| d\varsigma = (\xi_{n+1}-\xi'_m)\ln|\xi_{n+1}-\xi'_m| - (\xi_n-\xi'_m)\ln|\xi_n-\xi'_m| - \xi_{n+1}\ln|\xi_{n+1}| + \xi_n \ln|\xi_n| \tag{38}$$

$$\int_{\xi_n}^{\xi_{n+1}} (\varsigma-\xi_n)\ln\left|1-\frac{\xi'_m}{\varsigma}\right| d\varsigma = -\frac{1}{2}\xi'_m\Delta_\xi + \xi'_m(\xi_n-\frac{1}{2}\xi'_m)\ln\left|\frac{\xi_{n+1}-\xi'_m}{\xi_n-\xi'_m}\right| + \frac{1}{2}\xi_{n+1}(\Delta_\xi-\xi_n)\ln|(\xi_{n+1}-\xi'_m)/\xi_{n+1}| + \frac{1}{2}\xi_n^2\ln|(\xi_n-\xi'_m)/\xi_n| \tag{39}$$

It is seen that, at the centre of the contact patch (*i.e.* ξ_n or $\xi_{n+1}=0$) the last two terms in the right-hand side of equations (38) and (39) vanish. Equation (37) may be written in a compact form

$$u(\xi'_m,t) = \sum_{n=1}^{N} c_{mn} q(\xi_n,t) + u(0,t),\ (m=1,2,\cdots,N-1) \tag{40}$$

where c_{mn}'s are constant. Equation (40) gives

$$\frac{\partial u(\xi'_m,t)}{\partial t} = \sum_{n=1}^{N} c_{mn}\frac{\partial q(\xi_n,t)}{\partial t} + \frac{\partial u(0,t)}{\partial t},\ (m=1,2,\cdots,N-1) \tag{41}$$

Similarly for equation (30) and for $m=1,2,\cdots,N-1$,

$$\begin{aligned}\frac{\partial u(\xi'_m,t)}{\partial \xi} &= -\frac{4(1-\nu^2)}{\pi E}\sum_{n=1}^{N-1}\int_{\xi_n}^{\xi_{n+1}}\left\{q(\xi_n,t)+\frac{1}{\Delta_\xi}[q(\xi_{n+1},t)-q(\xi_n,t)](\varsigma-\xi_n)\right\}\frac{1}{\xi'_m-\varsigma}d\varsigma \\ &= -\frac{4(1-\nu^2)}{\pi E}\sum_{n=1}^{N-1}\left\{\begin{array}{l}\frac{1}{\Delta_\xi}[q(\xi_{n+1},t)-q(\xi_n,t)]\left[(\xi_n-\xi'_m)\ln\left|\frac{\xi_{n+1}-\xi'_m}{\xi_n-\xi'_m}\right|-\Delta_\xi\right] \\ -q(\xi_n,t)\ln\left|\frac{\xi_{n+1}-\xi'_m}{\xi_n-\xi'_m}\right|\end{array}\right\}\end{aligned} \tag{42}$$

or,

$$\frac{\partial u(\xi'_m,t)}{\partial \xi} = \sum_{n=1}^{N} d_{mn} q(\xi_n,t) \tag{43}$$

Inserting equations (40) to (43) into equation (26) yields

$$\begin{aligned}s(\xi'_m,t) &= V\gamma_1 - V\frac{\partial u(\xi'_m,t)}{\partial \xi} + \frac{\partial u(\xi'_m,t)}{\partial t} \\ &= V\gamma_1 - V\sum_{n=1}^{N} d_{mn} q(\xi_n,t) + \sum_{n=1}^{N} c_{mn}\frac{\partial q(\xi_n,t)}{\partial t} + \frac{\partial u(0,t)}{\partial t},\ (m=1,2,\cdots,N-1)\end{aligned} \tag{44}$$

Now it is assumed that the N_1 th displacement node is the slip-stick dividing node and there are $2N_s$ stress nodes outside of the contact patch. In the slip zone the tangential stress reaches the

maximum frictional stress and in the stick zone the slip velocity is vanishing. It is further assumed that *the tangential stress applied on the wheel in the contact patch is in the rolling direction.* Thus

$$q(\xi_n,t) = \mu_d\, p(\xi_n,t)\,,\ (n = N_s+1,\cdots N_1) \tag{45}$$

$$s(\xi'_m,t) = V\gamma_1 - V\sum_{n=1}^{N} d_{mn}\, q(\xi_n,t) + \sum_{n=1}^{N} c_{mn}\frac{\partial q(\xi_n,t)}{\partial t} + \frac{1}{\sigma}\frac{\partial q(0,t)}{\partial t} = 0\,,(m = N_1+1,\cdots N-N_s) \tag{46}$$

Using the approximation

$$\frac{\partial q(\xi,t)}{\partial t} \approx \frac{q(\xi,t)-q(\xi,t-\Delta t)}{\Delta t} \tag{47}$$

where, $V\times\Delta t$ must be much less than the shortest wavelength of the rail profile, equation (46) becomes

$$\begin{aligned}\sum_{n=N_1+1}^{N-N_s}\left(Vd_{mn}-\frac{c_{mn}}{\Delta t}\right)q(\xi_n,t) = V\gamma_1 + \mu_d\sum_{n=N_s+1}^{N_1}\left(\frac{c_{mn}}{\Delta t}-Vd_{mn}\right)p(\xi_n,t)\\ -\sum_{n=N_s+1}^{N-N_s}\frac{c_{mn}}{\Delta t}\,q(\xi_n,t-\Delta t) \qquad (m = N_1+1,\cdots N-N_s)\\ +\frac{1}{\sigma\Delta t}\,q(0,t)-\frac{1}{\sigma\Delta t}\,q(0,t-\Delta t)\end{aligned} \tag{48}$$

If the centre of the contact patch is in the slip zone, then $q(0,t) = \mu_d\, p(0,t)$, otherwise it is one of the unknowns governed by equation (48). From equation (48) $q(\xi_n,t)$ can be worked out for $n = N_1+1,\cdots,N-N_s$. The correct solution must satisfy $|\,q(\xi_n,t)\,| \le \mu_s\, p(\xi_n,t)$. If this condition is not fulfilled, then the division of the slip zone and stick zone is incorrect and a new division is assumed to perform another calculation. This procedure continues until the required condition is achieved.

It can be seen from equation (48) that to calculate the tangential stress at any time, an initial tangential stress must be given. In actual calculation, the initial tangential stress may be chosen to be that given by Carter [11]. Like the normal stress, the tangential stress is also a periodic function of time with the period being the sleeper-passing time. Example calculations show that this periodic solution can be achieved after having calculated for a single sleeper bay.

5. CALCULATION OF WEAR

Wear occurs in the slip zone. Wear at a position is assumed to be proportional to the work done by the tangential stress at that position over the time during which the position experiences slip. Since in the stick zone the slip velocity is zero, the change of the rail profile at position x can be calculated using the following formula

$$\Delta z(x) = \frac{1}{\rho}\int_{t_1}^{t_2} K \mid q(x,t)s(x,t) \mid dt \tag{49}$$

where, $[t_1, t_2]$ is the time period during which the position is in the nominal contact patch, *i.e.* $t_2 - t_1 = 2a_{\max}/V$, ρ is the mass density of the rail and K is a material related constant and is determined by experiment.

First the tangential stress and slip velocity are calculated for a number of discrete positions (called *the wear nodes*) defined by

$$x_k = (k-1)\Delta_\xi,\ k = 1, \cdots, \text{int}(L/\Delta_\xi) = N_x \tag{50}$$

They are fixed in a sleeper bay, and the wheel travels from a sleeper at $x_1 = 0$ to the next sleeper at $x_{N_x} = L$. Wear node x_k will be in the nominal contact patch when the wheel centre is at the following N wear node positions: $k - \frac{N-1}{2}$, $k - \frac{N-1}{2} + 1, \ldots\ k + \frac{N-1}{2}$. The stress node numbers for x_k are N, $N-1$, ... and 1, respectively. According to equation (49), the change of the rail profile at x_k can be approximated by

$$\Delta z(x_k) = \frac{K\Delta_\xi}{\rho V}\sum_{n=1}^{N} \mid q(\xi_n, t_n)s(\xi_n, t_n) \mid \tag{51}$$

where, if the time origin $t = 0$ corresponds to the wheel being at $x_1 = 0$, then

$$t_n = [(k-1) + \frac{N-1}{2} - n + 1)]\frac{\Delta_\xi}{V} \tag{52}$$

Now the discrete Fourier transform is performed on $\Delta z(x_k)$, giving the Fourier coefficients, ΔZ_k, of the height of the removed material by the lth wheel which has rolled over the sleeper bay. The fundamental wavenumber is given, according to the principle of the discrete Fourier transform, by $\frac{2\pi}{\Delta_\xi N_x} = \frac{2\pi}{L} = \beta_0$. Thus the rail profile after the passage of the lth wheel becomes (Note: ΔZ_0 must be set to be zero since it represents the average wear over the sleeper bay)

$$z_l(x) = \sum_{k=-\infty}^{\infty}(Z_k - \Delta Z_k)e^{ik\beta_0 x} \tag{54}$$

over which the next wheel will be rolling.

If $Z_k(m)$ denotes the rail roughness amplitude at wavenumber $k\beta_0$ after m passages of a wheel (or bogie), then a three-dimensional plot can be produced showing the roughness levels at

different wavenumbers and different numbers of passages of the wheel (or bogie). The slope along the passage axis shows the roughness growth rate at that wavenumber.

6. RESULTS

In this section, results are produced from the model, showing effects of various parameters on roughness growth or corrugation formation. Parameters having effects on rail roughness growth can be excitation frequency, train speed, initial roughness amplitude, railpad stiffness, number of wheels (single or multiple) and longitudinal creepage. Wheels from a British Class 87 electric locomotive are modelled as a rigid body having mass 1350 kg and a radius of 0.575 m. The static load applied by the wheel is identified to be 100 kN. The contact stiffness is evaluated to be 1.4×10^9 N/m. The rail is modelled as a Timoshenko beam. A set of typical parameters for the track structure is listed in Table 1. These parameters are for half the structure (*i.e.* a single rail on half sleepers) and correspond to a track with concrete sleepers and moderately stiff rail pads. In case of an initial roughness with a single wavelength, the amplitude of the roughness is chosen to be 10 μm (17 dB re 1 μm), *i.e.* $Z(x)=1\times10^{-5}\cos\frac{2\pi}{\lambda}x=1\times10^{-5}\cos\frac{2\pi f}{V}x$ (m) and $x=0$ is at a sleeper, where f denotes the excitation frequency, V the wheel speed and λ the wavelength. The longitudinal creepage between the wheel and rail is chosen to be 0.1%. The contact width is 16 mm (i.e. $b=8$ mm) and the friction coefficient is 0.3. And finally the value of K in equation (49) is chosen to be 2.5×10^{-9} kg/Nm [26].

TABLE 1 *Parameters for the vertical dynamics of a track*

Density of the rail	$\rho=7850$ kg/m^3
Young's modulus of the rail	$E=2.1\times10^{11}$ N/m^2
Shear modulus of the rail	$G=0.81\times10^{11}$ N/m^2
Loss factor of the rail	$\eta_R=0.01$
Cross-sectional area of the rail	$A=7.69\times10^{-3}$ m^2
Second moment of area of the rail cross-section	$I=30.55\times10^{-6}$ m^4
Shear coefficient of the rail cross-section	$\kappa=0.4$
Vertical rail pad stiffness	$k_{Pv}=3.5\times10^8$ N/m
Rail pad loss factor	$\eta_P=0.25$
Mass of sleeper	$m_S=162$ kg
Sleeper spacing	$l=0.6$ m
Vertical ballast stiffness	$k_{Bv}=50\times10^6$ N/m
Loss factor of ballast	$\eta_B=1.0$

6.1 CONTACT FORCE/STRESS AND SLIP VELOCITY

In this sub-section, results are presented for a single wheel moving at 40 m/s over the track. The aim is to give the general feature of contact and wear between a moving wheel and a track. Figures 8 and 9 show the 'position-histories' of the normal and tangential contact forces due to the wheel moving over the rail having roughness of wavelength 0.04 m. Therefore the excitation

frequency is 1000 Hz, close to the pinned-pinned frequency of the track. Although the roughness is sinusoidal, the contact force histories present a complex pattern. This is caused by the significant variation of the track dynamic stiffness at the pinned-pinned frequency along a sleeper bay. The average tangential contact force is about 7600 N, much less than the maximum frictional force ($0.3\times10^5 = 30$ kN), owing to the small creepage (0.1%). This average traction is balanced by the driving moment on the wheel. The dynamic components of the traction force will cause torsional vibration of the wheel on its axle. Torsional vibration of the wheel produces time-varying creepage in the longitudinal direction, and the amplitude of this time-varying creepage may exceed the rigid creepage when frequencies are close to the resonance frequencies of the wheelset. In other words, torsional vibration of the wheel must be considered in future work, although it is not included at the moment.

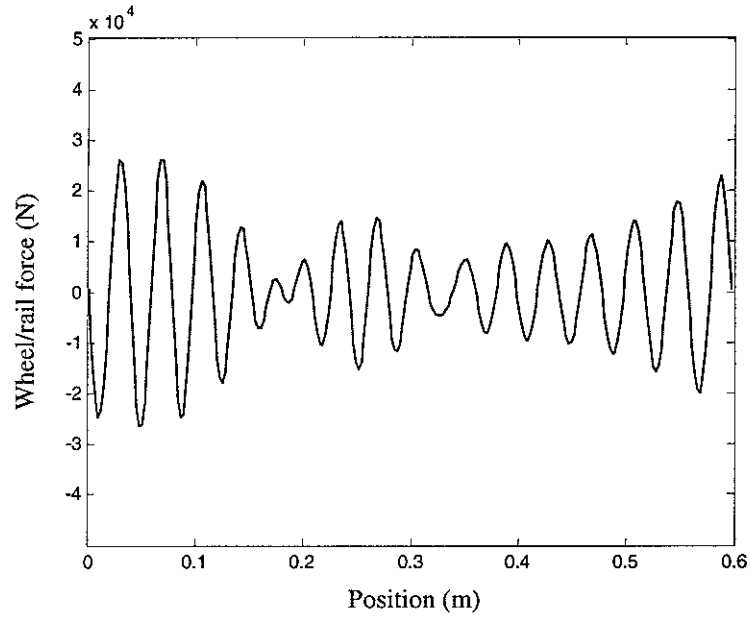

Figure 8. Position-history of the normal dynamic contact force for the wheel moving at 40 m/s over the rail with a sinusoidal railhead of amplitude 10 μm at a wavelength corresponding to 1000 Hz.

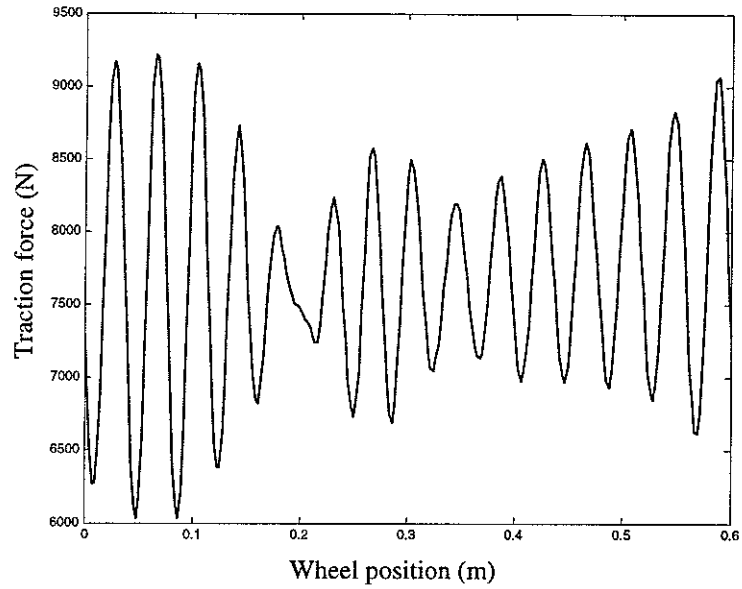

Figure 9. Position-history of the tangential contact force for the wheel moving at 40 m/s over the rail with a sinusoidal railhead of amplitude 10 μm at a wavelength corresponding to 1000 Hz.

Figure 10 and Figure 11 show the tangential contact stress and slip velocity at four instants within an excitation period (one millisecond). The contact lengths are less than 16 mm, much shorter than the wavelength of the roughness. Although the rigid creep velocity is 40×0.1% = 0.04 m/s, the slip velocity in the slip zone can be as high as 0.16 m/s. The slip velocity is largest at the trailing edge of the contact patch. Outside the contact patch the slip velocity is meaningless.

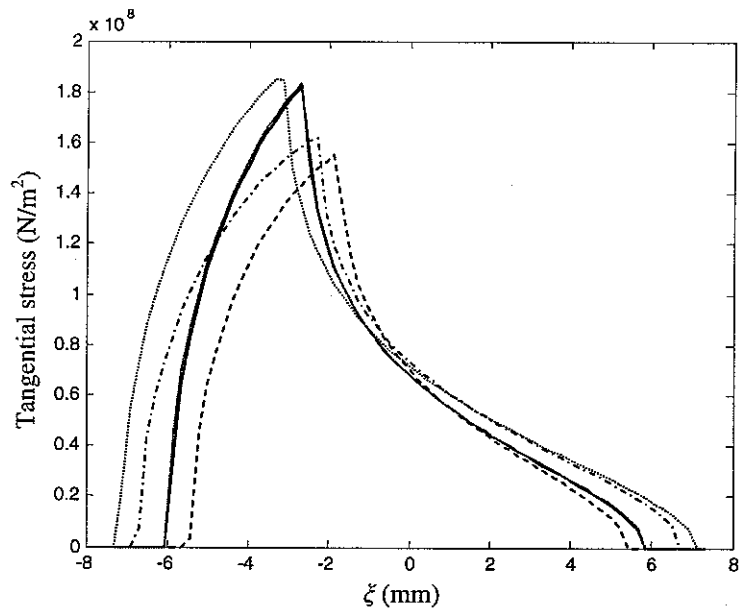

Figure 10. Tangential contact stress due to a single wheel moving at 40 m/s over the sinusoidal rail of wavelength 0.04 m. ——, $t = 0$; – – –, $t = 0.25$ ms ($x = 0.01$ m); – · –, $t = 0.5$ ms ($x = 0.02$ m); ……, t = 0.75 ms ($x = 0.03$ m); ——, $t = 1$ ms ($x = 0.04$ m).

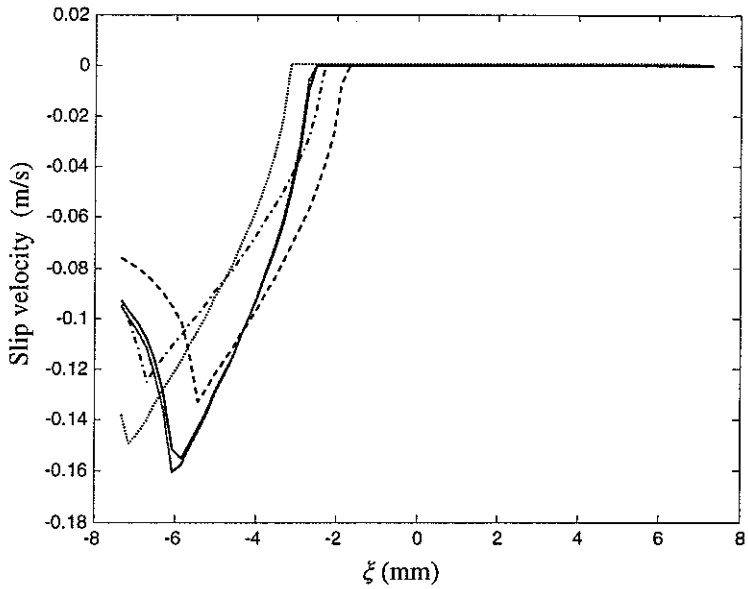

Figure 11. Slip velocity due to a single wheel moving at 40 m/s over the sinusoidal rail of wavelength 0.04 m. ——, $t = 0$; – – –, $t = 0.25$ ms ($x = 0.01$ m); – · –, $t = 0.5$ ms ($x = 0.02$ m); ....., t = 0.75 ms ($x = 0.03$ m); ——, $t = 1$ ms ($x = 0.04$ m). The slip velocity outside of the contact patch is meaningless.

6.2 WEAR AT DIFFERENT EXCITATION FREQUENIES

The height of the removed material (*i.e.* wear) after one passage of a single wheel and its wavenumber spectrum are shown in Figures 12 to 19 for initial wavelengths corresponding to 533 Hz, 1000 Hz, 1200 Hz and 1600 Hz. Figures 12, 14 and 16 show the position histories of the wear while others show the spectra of the wear for positive wavenumbers up to 525 rad/m. The wheel speed is 40 m/s and these frequencies correspond to wavelengths of 0.075 m, 0.04 m, 0.03 m and 0.025 m. At these wavelengths, the levels of roughness equivalent to the parametric excitation [19] are much lower than the assumed roughness level which is 17 dB.

For excitation frequencies much less or greater than the pinned-pinned frequency (Figures 12 and 18), wear is basically harmonic of the same wavelength as the initial roughness if the uniform part is subtracted. Maximum wear occurs at the trough of the initial roughness while minimum wear occurs at its crest. This is consistent with what is observed *in situ*. Therefore the initial roughness grows. At the troughs the normal wheel/rail force is not necessarily the minimum.

Around the pinned-pinned frequency, the wear pattern is complicated (Figures 14 and 16). Figure 14 for 1000 Hz still presents features similar to those identified above: more wear occurs at the trough of the initial roughness than at the crest. Roughness grows more quickly around a sleeper than around the mid-span. However, at 1200 Hz (Figure 16) and at a sleeper, more wear occurs at the crest of the initial roughness. This implies that at a sleeper the roughness will be depressed. However, away from the sleepers, the peak wear still occurs at the trough of the initial roughness.

This observation seems to indicate that corrugation is more likely to form near a sleeper and the wavelength of the corrugation is determined by the pinned-pinned frequency.

For a given amplitude of initial roughness, Figures 12, 14, 16 and 18 show that roughness corresponding to the pinned-pinned frequency grows faster than that corresponding to other frequencies. This observation is consistent with that from previous studies.

From Figures 13, 15, 17 and 19 it is seen that, in addition to roughness growth at the original wavelength, roughness at other wavelengths, especially at that equal to the sleeper-spacing (wave number 10 rad/m) and half the original wavelength (twice the original wavenumber), is also produced by the moving wheel. Roughness growth at a wavelength equal to the sleeper spacing depends only slightly on the excitation frequency. This is because it is mainly caused by the parametric excitation of the moving wheel. Roughness growth at half the original wavelength is the result of the friction work, which is assumed to be proportional to the wear and done by the dynamic tangential contact stress on the dynamic slip velocity (the product of two harmonic functions of the same frequency is a function of twice the frequency). It is noticed that, as the original wavelength decreases, roughness growth at half the original wavelength increases.

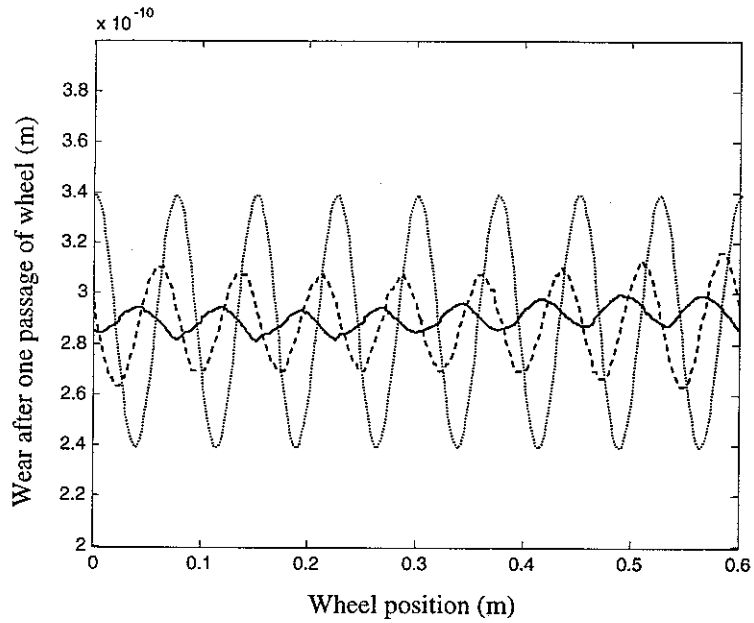

Figure 12. Wear (——) after one passage of wheel over the initial roughness (……, not in scale). Wheel speed 40 m/s, excitation frequency 533 Hz. Also shown is the normal dynamic contact force history (– – –, not in scale).

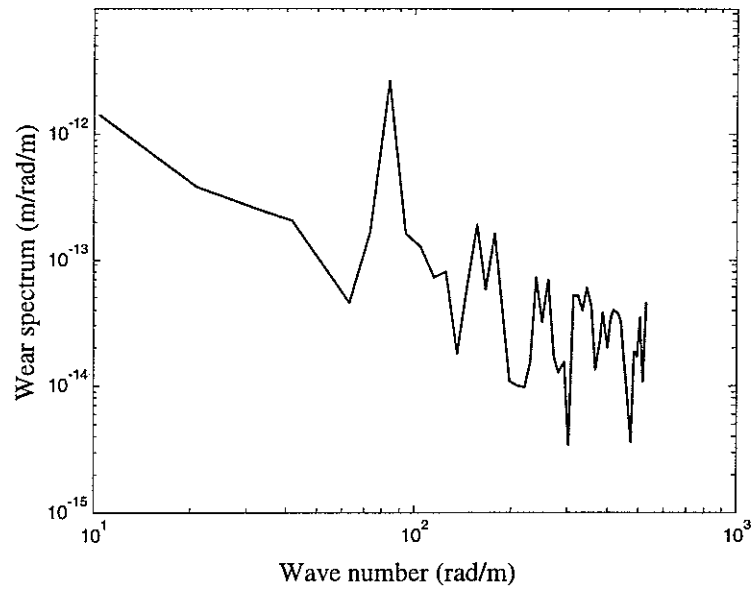

Figure 13. Spectrum of the wear after one passage of wheel. Wheel speed 40 m/s, excitation frequency 533 Hz. The peak occurs at the wavenumber of the initial roughness (84 rad/m).

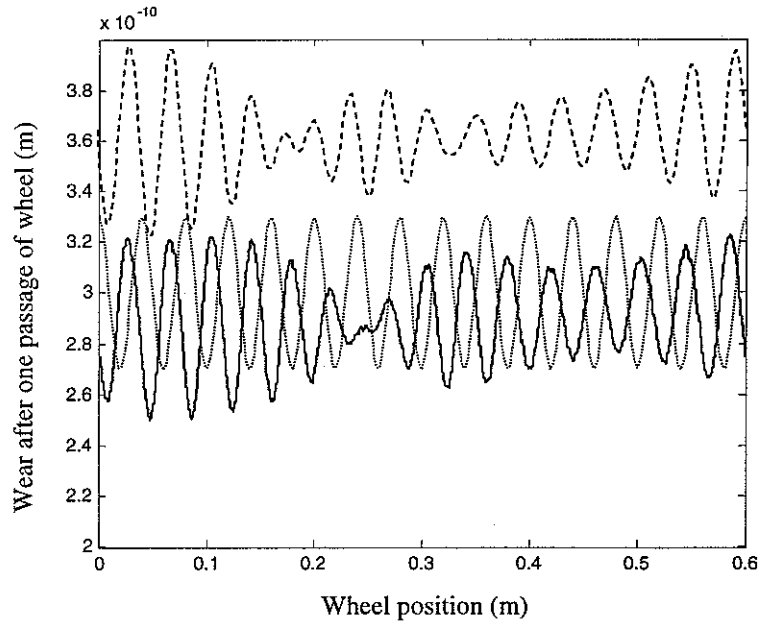

Figure 14. Wear (——) after one passage of wheel over the initial roughness (……, not in scale). Wheel speed 40 m/s, excitation frequency 1000 Hz. Also shown is the normal dynamic contact force history (– – –, not in scale).

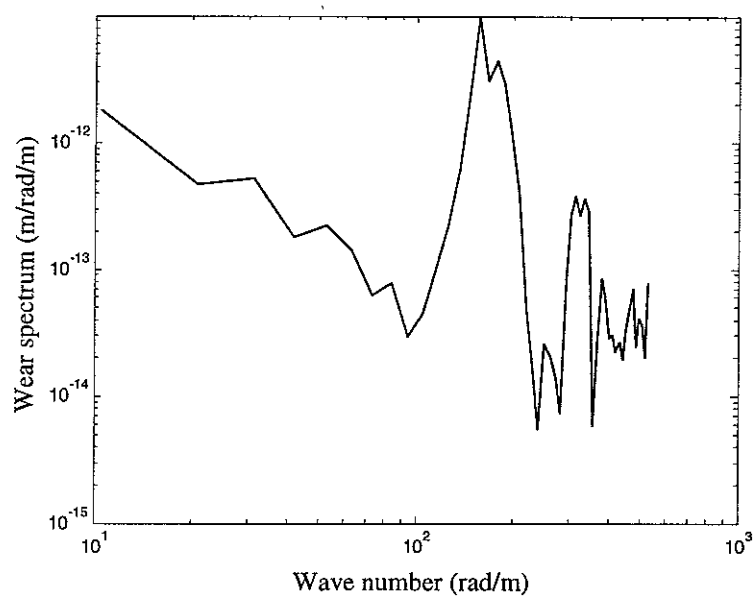

Figure 15. Spectrum of wear after one passage of wheel. Wheel speed 40 m/s, excitation frequency 1000 Hz. The highest peak occurs at the wavenumber of the initial roughness (157 rad/m).

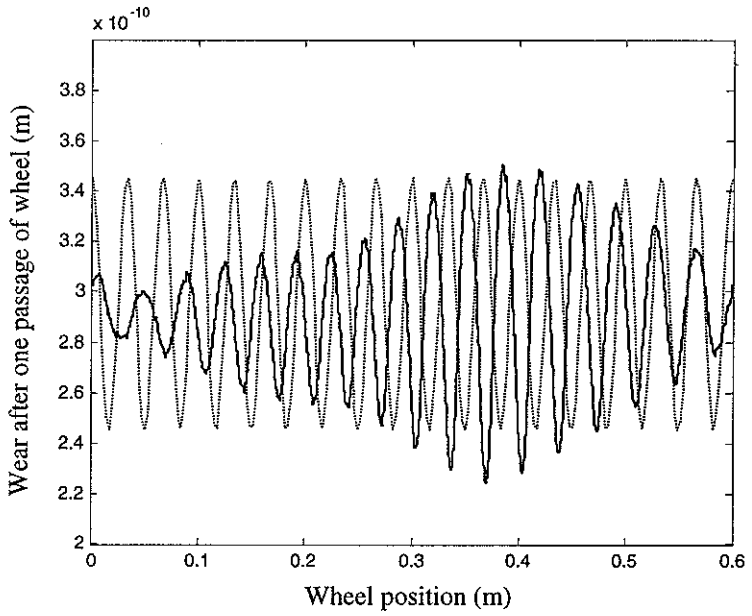

Figure 16. Wear (——) after one passage of wheel over the initial roughness (……, not in scale). Wheel speed 40 m/s, excitation frequency 1200 Hz.

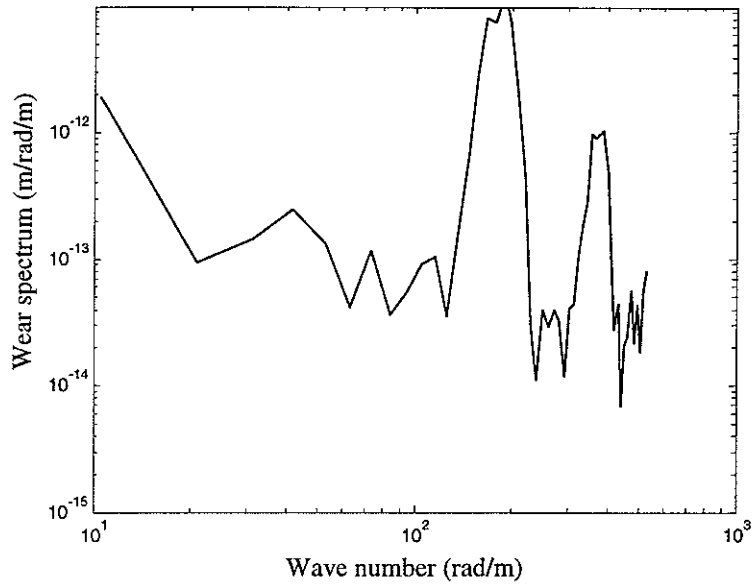

Figure 17. Spectrum of wear after one passage of wheel. Wheel speed 40 m/s, excitation frequency 1200 Hz. The highest peak occurs at the wavenumber of the initial roughness (188 rad/m).

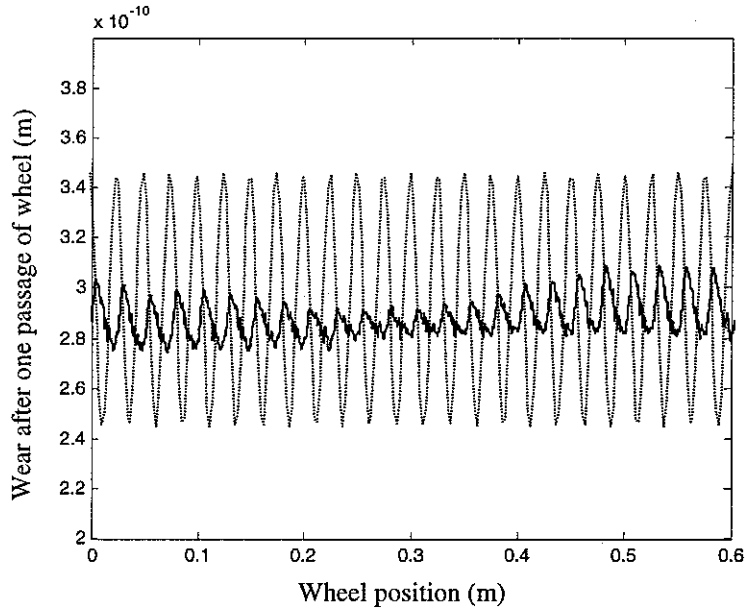

Figure 18. Wear (——) after one passage of wheel over the initial roughness (……, not in scale). Wheel speed 40 m/s, excitation frequency 1600 Hz.

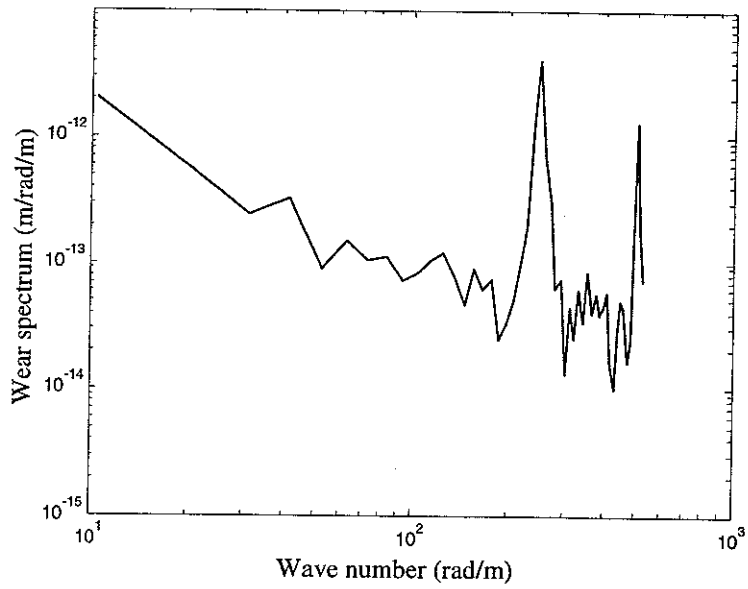

Figure 19. Spectrum of wear after one passage of wheel. Wheel speed 40 m/s, excitation frequency 1600 Hz. The highest peak occurs at the wavenumber of the initial roughness (251 rad/m).

6.3 EFFECT OF WHEEL SPEED ON ROUGHNESS GROWTH

Due to the varying stiffness of the track, roughness can be developed from an absolutely smooth rail. This is demonstrated in Figures 20 and 21 for wheel speeds of 20 m/s and 40 m/s respectively. Each curve in these graphs represents the rail profile after a particular number of passages of a wheel. The number of wheel passages between each pair of adjacent profiles is 10000. Starting from a smooth rail, roughness grows particularly at the wavelength of the sleeper spacing. Roughness at shorter wavelengths, corresponding to anti-resonances of the rail, is developed simultaneously. For the wheel moving at 20 m/s, roughness at a wavelength of about 0.1 m is developed just after a sleeper. This wavelength corresponds to the high stiffness of the rail at about 200-300 Hz at which sleepers vibrate as dynamic absorbers to the rail. At 40 m/s, roughness of about 0.03-0.04 m is clearly shown in Figure 21 and it corresponds to the pinned-pinned frequency. These two figures show that roughness of short wavelengths spreads from sleepers to the mid-span as wheel speed increases.

It is noted from these two figures that there are positions where the wear is always equal to the average wear in a sleeper bay and therefore the height of the roughness at these positions is zero after each passage of the wheel. This may be explained by the fact that the dynamic wheel/rail force from the parametric excitation, which is dominant over the dynamic wheel/rail force caused by the newly produced roughness [19], disappears at these positions, as shown in Figure 22. Comparison of Figures 20 and 21 with Figure 22 shows that lower normal wheel/rail force corresponds to more

removal of material from the railhead. This is because for a given creepage, lower normal wheel/rail force results in a greater slip zone in the contact patch.

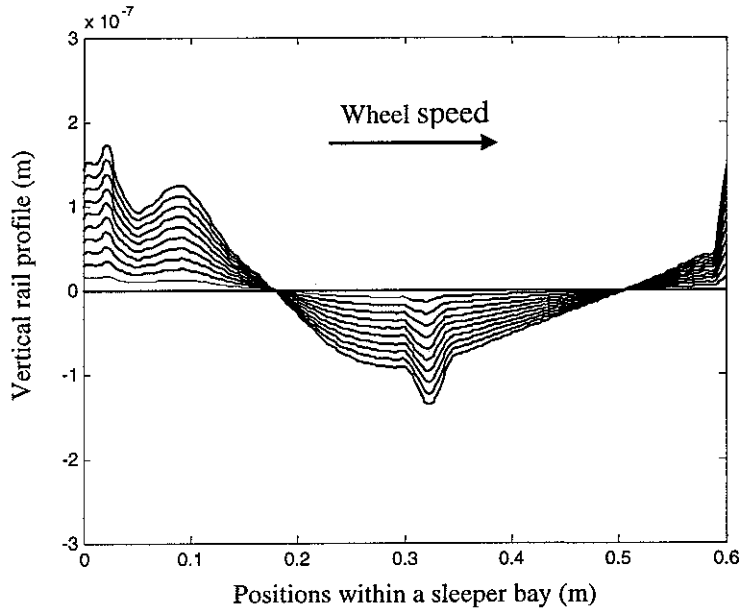

Figure 20. Rail roughness evolution from a smooth rail. Wheel speed 20 m/s.

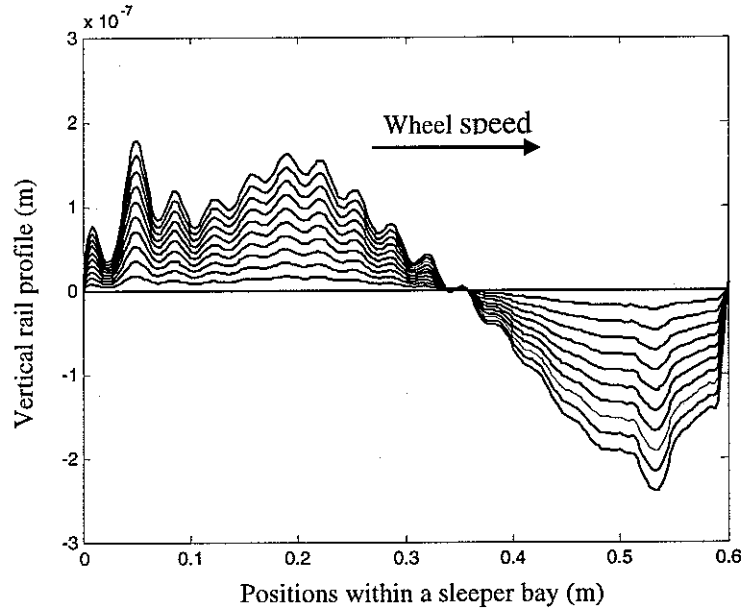

Figure 21. Rail roughness evolution from a smooth rail. Wheel speed 40 m/s.

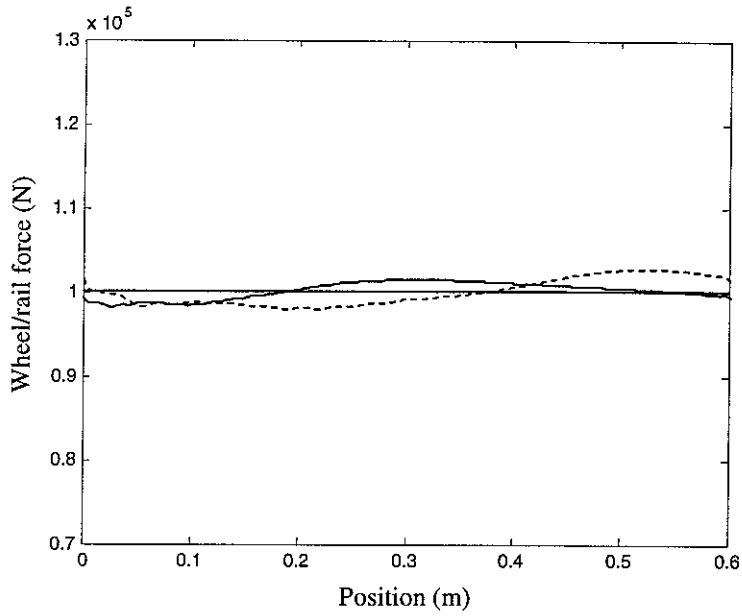

Figure 22. Wheel/rail force position-history for the wheel moving at 20 m/s (——) and 40 m/s (– – –) over the rail with a smooth railhead.

The observations made above can also be made from the spectrum shown in Figure 23 of the rail roughness produced by 100,000 wheel passages from a smooth rail for four wheel speeds (20 m/s, 40 m/s, 60 m/s and 80 m/s). Symbols are placed on peaks and dips. Symbols of the same shape and colour on different curves indicate that the marked peaks/dips correspond to the same characteristic frequency of the track.

It can be seen that, roughness components at wavelengths of the sleeper spacing (wavenumber 10 rad/m) and a half and a third of this increase with wheel speed and are dominant. These components are produced by the parametric excitation of the moving wheel.

At 20 m/s, four points, A, B, C and D, are identified. The dips A and C correspond to the low vertical stiffness of the rail at frequencies about 100 Hz (resonance of the track mass on the ballast) and 500 Hz (resonance of the rail and sleeper out-of-phase). The peak B at a wavenumber of about 80 rad/m is caused by the high stiffness of the rail at about 200-300 Hz at which sleepers vibrate as absorbers to the rail. This roughness component is much more significant near a sleeper (Figure 20). The point D corresponds to the pinned-pinned vibration and does not appear as a peak. This is because at this wheel speed the wavelength corresponding to the pinned-pinned frequency is less than 0.02 m and the roughness component at this wavelength is filtered to a large extent by the wheel/rail contact patch. However at higher wheel speeds, short wavelength roughness corresponding to the pinned-pinned frequency becomes significant. This is also shown in Figure 21.

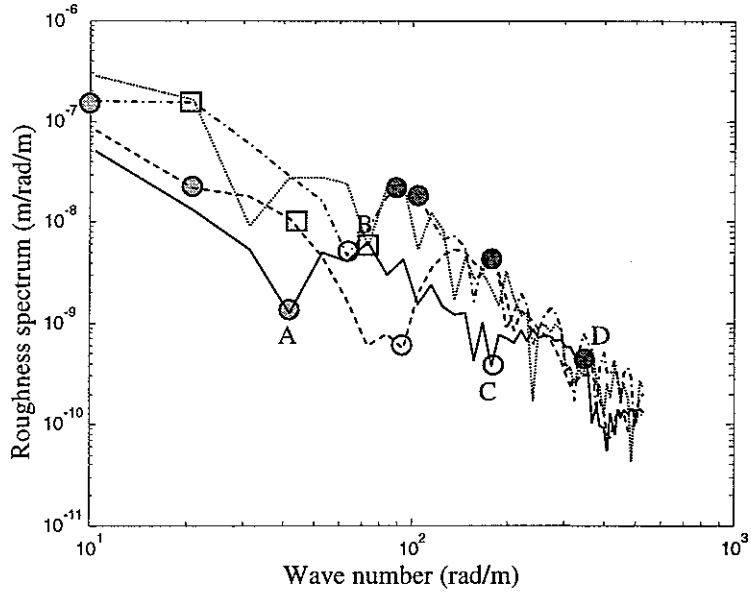

Figure 23. Spectrum of the rail roughness produced by 100,000 wheel passages from a smooth rail. ——, wheel speed 20 m/s; – – –, wheel speed 40 m/s; – · –, wheel speed 60 m/s; ....., wheel speed 80 m/s. Symbols of the same shape and colour at different curves indicate that the peaks/dips are corresponding to the same characteristic frequency of the track.

The above observations show the importance of the parametric excitation in roughness growth and explain why short pitch corrugation is commonly associated with high-speed, main-line track.

6.4 EFFECT OF RAILPAD STIFFNESS ON ROUGHNESS GROWTH

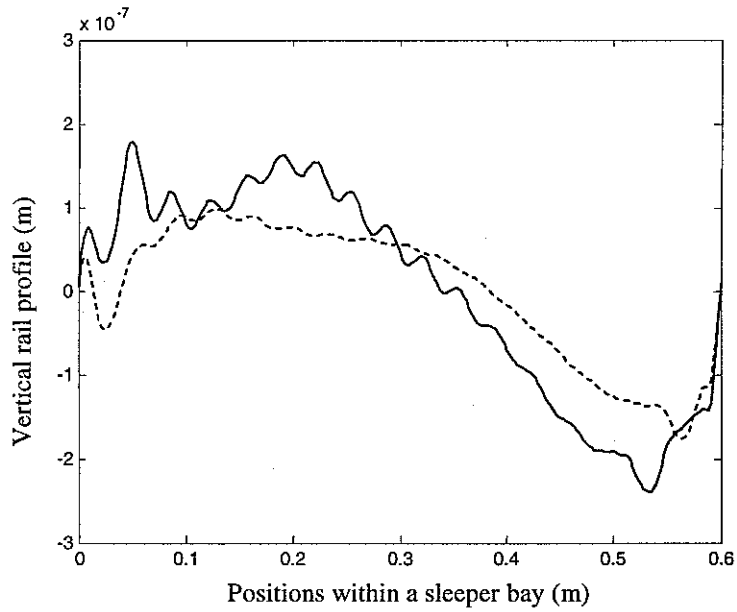

Figure 24. Rail roughness produced by 100,000 wheel passages at 40 m/s from a smooth rail. ——, railpad stiffness 3.5×10^8 N/m; – – –, railpad stiffness 0.7×10^8 N/m.

The effect of the rail pad stiffness is demonstrated in Figures 24 and 25. Figure 24 shows the rail profile produced from a smooth rail after 100,000 passages by a single wheel moving at 40 m/s. The wavenumber spectrum of the profile is shown in Figure 25. Two values of railpad stiffness, 3.5×10^8 N/m and 0.7×10^8 N/m, are examined while other parameters are listed in Table 1. It can be seen that, for most of the wavelengths, the softer rail pad reduces roughness growth, resulting in a lower overall roughness level (Figure 24). The prominent peak for the stiffer rail pad at a wavelength (about 0.33 m) corresponding to the pinned-pinned frequency is reduced by the reduction in rail pad stiffness and becomes broader and smoother, indicating corrugation at that wavelength is much less evident. In other words, soft rail pads can prevent corrugation formation.

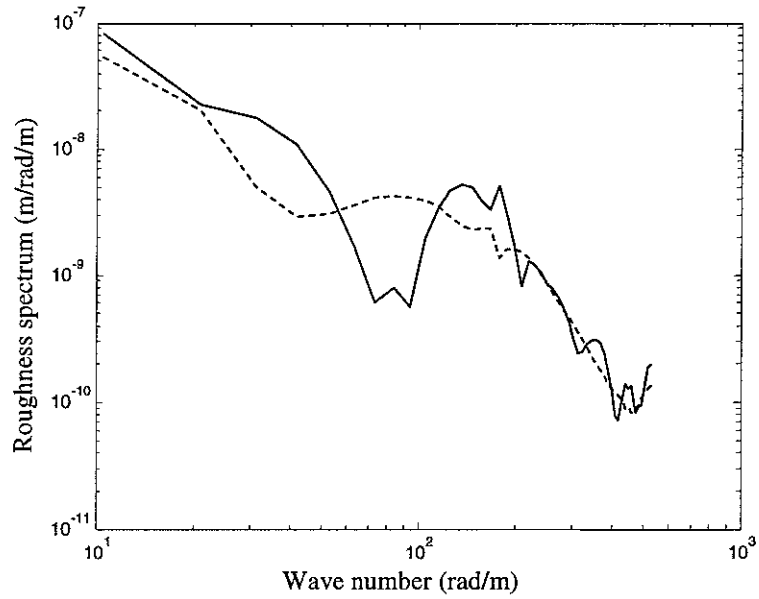

Figure 25. Spectrum of the rail roughness produced by 100,000 wheel passages at 40 m/s from a smooth rail. ——, railpad stiffness 3.5×10^8 N/m; – – –, railpad stiffness 0.7×10^8 N/m.

6.5 EFFECT OF MULTIPLE WHEELS

The above results have been presented for a single wheel. In other words, for each passage there is only a single wheel moving along the track, excluding the effects from adjacent wheels in a bogie. As shown in references [15, 19], normal wheel/rail force at a wheel can be affected by other wheels, especially at excitation frequencies at which interference occurs between the wheels. Figures 26 and 27 show the effects of the presence of multiple wheels on roughness growth. Here four driving wheels from two bogies in a British Class 87 electric locomotive are present for each passage. The bogie wheelbase is 3.3 m long and the distance between the bogie centres is 10 m. The main effect is that the multiple wheels model reduces roughness growth compared with a single wheel model. This may be explained by the fact that maximum wear occurs at different positions for different wheels. Compared to the single wheel model, the multiple wheels model produces

extra dips and peaks. These peaks and dips are caused by the interferences between the wheels, and the corresponding wavelengths are determined by, among other things, the separations of the wheels.

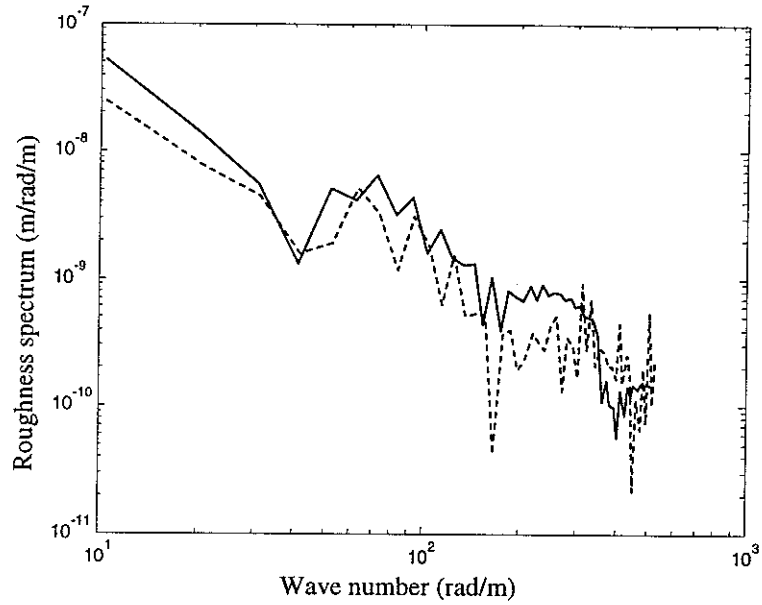

Figure 26. Spectra of the rail roughness produced by 100,000 wheel passages from a smooth rail with wheel speed being 20 m/s. ——, single wheel model; – – –, multiple (four) wheel model (one passage of the two bogie equals four wheel passages).

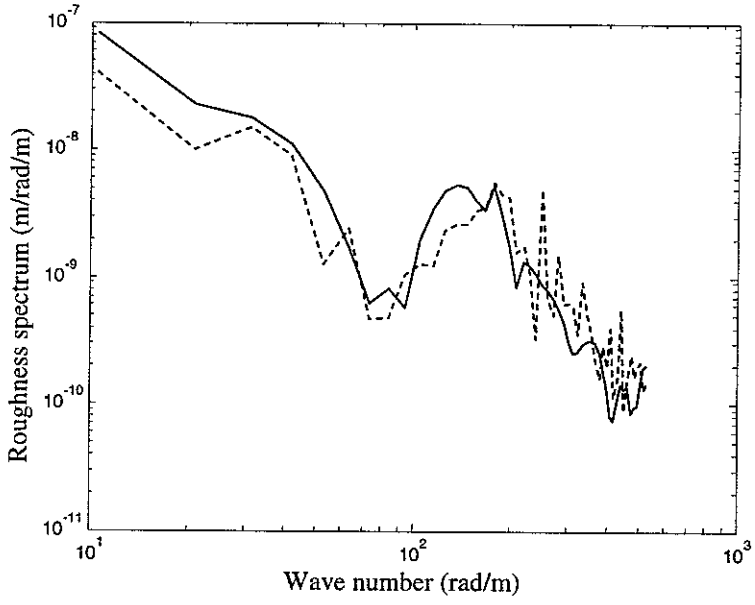

Figure 27. Spectra of the rail roughness produced by 100,000 wheel passages from a smooth rail with wheel speed being 40 m/s. ——, single wheel model; – – –, multiple (four) wheel model (one passage of the two bogie equals four wheel passages).

7. CONCLUSIONS

An investigation into rail roughness growth is presented which overcomes shortcomings found in previous studies. Using the wavenumber-based calculation method for the response of a periodically supported rail to a moving static or harmonic load, dynamic wheel/rail forces are calculated for multiple wheels moving over an initially rough or smooth rail. By assuming wear is the only damage mechanism, removal of material from the rail rolling surface is evaluated using the two-dimensional unsteady contact mechanics theory. A great number of repetitions of such a process demonstrate how rail roughness grows and corrugation forms. Discussion is also given to the accuracy of using the half-space theory to approximate the deformation in a contact patch. It is shown that damping may be introduced into the Hertz contact spring for the dynamic case.

Results from the roughness growth prediction model show that,

1. Parametric excitation has significant contribution to the initiation of rail roughness;

2. The amount of roughness growth depends strongly on excitation frequency. Near the pinned-pinned frequency, maximum wear occurs;

3. Short wavelength roughness grows from just after the sleepers. As wheel speed increases, short wavelength roughness spreads to the mid-span;

4. Low railpad stiffness can reduce roughness growth;

5. The multiple-wheel model predicts less roughness than the single-wheel model;

ACKNOWLEDGEMENT

This work is supported by the EPSRC and Rail Research UK under project A3: *Railway noise: curve squeal, roughness growth, friction and wear.*

REFERENCES

[1] K. L. Johnson, 1987 *Contact Mechanics*, Cambridge University Press.

[2] S. L. Grassie and J. Kalousek 1993 *Proceedings of the Institute of Mechanical Engineers* **207**, *Part F: Journal of Rail and Rapid Transit*, 57-68. Rail corrugation: characteristics, causes and treatments.

[3] Y. Sato, A. Matsumoto and K. Knothe 2002 *Wear* **253**, 130-139. Review on rail corrugation studies.

[4] S. L. Grassie 2003 *Proceedings of the 6th International Conference on Contact Mechanics and Wear of Rail/Wheel Systems*, Gothenburg, Sweden, 11-19. Rail corrugation: advances in measurement, understanding and treatment.

[5] S. Müller 1999 *Journal of Sound and Vibration* **227**(5), 899-913. A linear wheel-track model to predict instability and short pitch corrugation, 181-211.

[6] K. Knothe 2000 *Rolling Contact Phenomena. CISME Courses and Lectures*, No. 411, 203-276, Springer, New York. Chapter 4 on non-steady state rolling contact and corrugations.

[7] A. Valdivia 1987 *PhD Dissertation, TU Berlin.* Interaction between high-frequency wheel-rail dynamics and irregular rail wear—a linear model.

[8] K. Hempelmann and K. Knothe 1996 *Wear* **191**, 161-169. An extended linear model for the prediction of short-pitch corrugation.

[9] C. O. Frederick 1986 *Proceedings of the Second Conference on the Contact Mechanics and Wear of Rail/Wheel Systems*, A rail corrugation theory.

[10] J. B. Nielsen 1999 *Journal of Sound and Vibration* **227**(5), 915-933. Evolution of rail corrugation predicted with a non-linear wear model.

[11] F. W. Carter 1926 *Proceedings of the Royal Society of London*, **A112**, 151-157. On the action of a locomotive driving wheel.

[12] J. Piotrowski and J. J. Kalker 1993. In *Contact Mechanics—Computational Techniques* (M. H. Aliabadi and C. A. Brebbia, editors), First International Conference on Contact Mechanics, 413-424, Southampton.

[13] J. J. Kalker 1990 *Three-Dimensional Elastic Bodies in Rolling Contact.* Kluwer Academic Publishers.

[14] H. Ilias 1999 *Journal of Sound and Vibration* **227**(5), 935-948. The influence of railpad stiffness on wheel/track interaction and corrugation growth.

[15] T. X. Wu and D. J. Thompson 2002 *Vehicle System Dynamics* **37**, 157-174. Behaviour of the normal contact force under multiple wheel/rail interaction.

[16] T. X. Wu and D. J. Thompson 2003 *Proceedings of the 6th International Conference on Contact Mechanics and Wear of Rail/Wheel Systems (CM2003)*, Gothenburg, Sweden. An investigation into rail corrugation due to micro-slip under multiple wheel/rail interactions.

[17] C. Andersson 2003 *PhD Thesis, Chalmers University of Technology*. Modelling and simulation of train-track interaction including wear prediction.

[18] X. Sheng, C. J. C. Jones and D. J. Thompson. Responses of infinite periodic structures to moving or stationary harmonic loads. Accepted by *Journal of Sound and Vibration*.

[19] X. Sheng, D. J. Thompson and C. J. C. Jones 2004 *Proceedings of IOA Spring Conference*, 29-30 March, Southampton. Interactions between a single moving wheel and a periodically supported rail.

[20] J. J. Kalker 1979 *International Journal of Numerical Methods for Engineering*, **14**, 1293-1307. The computation of three-dimensional rolling contact with dry friction.

[21] E. A. H. Vollebregt, J. J. Kalker and G. Wang CONTACT'93 Users manual.

[22] J. J. Kalker 1971 *Transactions of the ASME, Journal of Applied Mechanics*, **38**, 875-887. A minimum principle for the law of dry friction, with application to elastic cylindrical in rolling contact, Parts 1, 2.

[23] J. Dominguez 1993, *Boundary Elements in Dynamics*, Elsevier Applied Science.

[24] X. Sheng, C.J.C. Jones and M. Petyt 1999 *Journal of Sound and Vibration* **225**(1), 3-28. Ground vibration generated by a harmonic load acting on a railway track.

[25] S. L. Grassie and K. L. Johnson 1985 *Wear* **101**, 291-309. Periodic microslip between a rolling wheel and a corrugated rail.

[26] J. C. O. Nielsen 2003 *Journal of Sound and Vibration* **267**(3), 537-548. Numerical prediction of rail roughness growth on tangent tracks.